A Review on Convergence Properties and Spectral Properties of SEM and IGA approximations

Ondine Chanon[1], Luca Dedè[2], Paola Gervasio[3], and Alfio Quarteroni[1,2]

[1]CMCS, Institute of Mathematics, École Polytechnique Fédérale de Lausanne, Station 8, CH-1015 Lausanne, Switzerland
[2]MOX, Politecnico di Milano, P.zza Leonardo da Vinci 32, Milano, 20133, Italy
[3]DICATAM, Università degli Studi di Brescia, via Branze 38, I-25123 Brescia, Italy

July 9, 2017

Abstract

This paper introduces a systematic comparison of the theoretical properties of Spectral Elerment Methods (SEM) and Isogeometric Analysis (IGA), with a specific attention payd to their convergence properties, the algebraic pattern and the spectral properties of the corresponding arrays (mass and stiffness matrices). Available theoretical results are supported by numerical evidence. Where theory is lacking, numerical investigation allows us to draw a conjecture on the behavior of the corresponding theoretical laws in terms of the design parameters, such as the element size, the local polynomial degree, the space dimension, the total number of degrees of freedom (i.e. the array size).

Keywords. isogeometric analysis, *hp* finite element methods, spectral element methods, convergence, condition number

1 Introduction

Spectral element methods (SEM) (see, e.g., [8]) and Isogeometric Analysis (IGA) (see, e.g., [14]) represent two different paradigms for high order approximation of partial differential equations (PDEs). Apart from their different use of basis functions, piecewise polynomials for SEM, piecewise NURBS for IGA (with variable degree of continuity across element boundaries), the two approaches share many similarities.

The perhaps more remarkable are reported below:

1 – they are both Galerkin methods: SEM is however most often used with inexact calculation of integrals using the so-called Gauss-Legendre-Lobatto numerical integration. This results into the so-called SEM-NI method (NI standing for numerical integration);

2 – the induced approximation error decays more than algebraically fast with respect to the local polynomial degree.

On the other hand, the two approaches differ in what concern the algebraic structures of the corresponding arrays (say, the mass and the stiffness matrices), the spectral properties of the latter (the behavior of their extreme eigenvalues, and the corresponding condition number), and the actual decay rate of the approximation error with respect to the discretization parameters: the element-size h, and the local polynomial degree p.

Our aim in this note is to report on the most relevant theoretical results addressing the issues above. Most of these results are taken from the existing literature, few of them are new. (Paola: per la parte di convergenza sono d'accordo, c'è solo un teorema di convergenza per $s \geq p + 1$ e $p \geq 2k - 1$. Per la parte sugli autovalori forse non sono proprio così pochi, tutti gli andamenti degli autovalori IGA sono nuovi, non ci sono in letteratura. Qui potremmo espandere meglio)

When the theory is missing we investigate these properties numerically and we propose the law of behavior in terms of h, p, the spatial dimension d, and the total number of degrees of freedom d.o.f.

Our analysis is concerned with the approximation of the mass matrix and the stiffness matrix for the Poisson boundary value problem in a cubic domain. We systematically compare SEM-NI with two reealization of IGA: IGA-C^0 (the continuity across interelement boundaries is only imposed on the problem solution) and IGA-C^{p-1} (the continuity holds for the solution as well as for all its derivatives of order up to $p - 1$).

Vogliamo anticipare qualche conclusione? ci provo, ma dobbiamo stare attenti nella sintesi a non essere troppo imprecisi se no il glorioso popolo di IGA si ribella. Alternativa: non si mette alcuna anticipazione qui, ma si riportano invece nelle conclusioni in modo piu' analitico, punto per punto

In general terms we can concude that, errorwise, IGA-C^0 and SEM-NI behave essentially in the same way, whereas IGA-C^{p-1} converges faster with respect to the polynomial degree. The latter is also the most accurate when the error is plotted against d.o.f.

On a different side, SEM-NI arrays are in general less dense and better conditioned with respect to those of IGA-C^{p-1}.

A specific outile of the paper is as follows.

qui lista dei contenuti

concluderei dicendo qualcosa del genere:

This review contains for the first time a systematic comparison of the theoretical properties of two classes of methods that are very popular and highly appreciated in the community of numerical analysts and computational scientists. We are confident that this analysis will be useful for a comparative assessment of the two approaches and a better and more awareful appreciation of their qualities and their limitations.

2 Problem setting

Let $\Omega = (0,1)^d$, with $d = 1, 2, 3$, be the computational domain, $f \in L^2(\Omega)$ be a given function. Our reference Poisson problem reads

$$\begin{cases} -\Delta u = f & \text{in } \Omega \\ u = 0 & \text{on } \partial\Omega. \end{cases} \tag{1}$$

2

The weak form of problem (1) reads: look for $u \in V = H_0^1(\Omega)$ s.t.

$$a(u,v) = \mathcal{F}(v) \qquad \forall v \in V, \tag{2}$$

where $a(u,v) = \int_\Omega \nabla u \cdot \nabla v \, d\Omega$ and $\mathcal{F}(v) = \int_\Omega fv \, d\Omega$. Problem (2) admits a unique solution (see, e.g., [17]) that is stable w.r.t. the data f.

2.1 Discretization by the Spectral Element Method (SEM)

Given $h > 0$, let $\mathcal{T}_h$ be a family of partitions of the computational domain $\Omega \subset \mathbb{R}^d$ in quads (intervals when $d = 1$, quadrilaterals when $d = 2$ and hexaedra when $d = 3$). Following standard assumptions we require $\mathcal{T}_h$ to be affine, regular, and quasi-uniform (see [17, Ch. 3]). The affinity assumption implies that in fact our partition is made of rectangles when $d = 2$ and parallelepipedon when $d = 3$. We denote by $\hat{T}$ the reference element, i.e. the $d-$dimensional cube $(-1,1)^d$ and each element $T_k \in \mathcal{T}_h$ is the affine transformation of the reference element $\hat{T}$ through the affine map $\mathbf{F}_k$. We suppose that the mesh is conformal, i.e., two adjacent elements of $\mathcal{T}_h$ share either a common vertex, or a complete edge, or else a complete face (when $d = 3$). Finally, under the assumption that the mesh is uniform, we denote by n the number of elements along each direction so that $h \sim 1/n$. The global number of elements is $N = n^d$.

Formulation

Given an integer $p \geq 1$, let us denote by $\mathbb{Q}_p$ the space of polynomials of degree less than or equal to p with respect to each variable $x_1, \dots, x_d$. We introduce the following finite dimensional spaces in $\overline{\Omega}$:

$$X_\delta = \{v \in C^0(\overline{\Omega}) : v_{|T_k} \in \mathbb{Q}_p \circ \mathbf{F}_k^{-1}, \, \forall T_k \in \mathcal{T}_h\}, \qquad V_\delta = V \cap X_\delta. \tag{3}$$

δ is an abridged notation undermining the mesh size h and the local polynomial degree p.

The Galerkin approximation of (2) reads: look for $u_\delta \in V_\delta$ s.t.

$$a(u_\delta, v_\delta) = \mathcal{F}(v_\delta) \qquad \forall v_\delta \in V_\delta. \tag{4}$$

Typically, when using SEM, the exact integrals appearing in a and $\mathcal{F}$ are replaced by the composite Legendre-Gauss-Lobatto (LGL) quadrature formulas (see [7]) with the aim of reducing the computational effort.

For any integer $p \geq 1$, the $(p+1)$ LGL nodes and weights are first defined on the reference interval $(-1,1)$ (see [7, formula (2.3.12)]) and then tensorized and mapped into the generic quad $T_k \in \mathcal{T}_h$ by applying the affine map $\mathbf{F}_k$. Let $\mathbf{x}_q^{(k)}$ and $w_q^{(k)}$, with $q = 1, \dots, (p+1)^d$ denote the quadrature nodes and weights on T_k for any $T_k \in \mathcal{T}_h$. By setting

$$a_\delta(u_\delta, v_\delta) \;=\; \sum_{k=1}^{N} \sum_{q=1}^{(p+1)^d} \nabla u_\delta(\mathbf{x}_q^{(k)}) \cdot \nabla v_\delta(\mathbf{x}_q^{(k)}) w_q^{(k)}, \tag{5}$$

$$\mathcal{F}_\delta(v_\delta) \;=\; (f, v_\delta)_\delta = \sum_{k=1}^{N} \sum_{q=1}^{(p+1)^d} f(\mathbf{x}_q^{(k)}) v_\delta(\mathbf{x}_q^{(k)}) w_q^{(k)}, \tag{6}$$

3

the discrete Galerkin formulation of (2) with Numerical Integration (SEM-NI) reads: look for $u_\delta \in V_\delta$ s.t.

$$a_\delta(u_\delta, v_\delta) = \mathcal{F}_\delta(v_\delta) \qquad \forall v_\delta \in V_\delta. \tag{7}$$

Error estimates

The quadrature error produced by the LGL formulas decays with *spectral* accuracy, i.e., there exists $c = c(\Omega) > 0$ such that, for any $f \in H^s(\Omega)$, with $s \geq 1$, and for any $v_\delta \in V_\delta$ it holds (see [7, Sect. 5.4.3] and standard scaling arguments)

$$|(f, v_\delta) - (f, v_\delta)_\delta| \leq c(\Omega) p^{-s} h^s \|f\|_{H^s(\Omega)} \|v_\delta\|_{L^2(\Omega)}. \tag{8}$$

Using (8) and the Strang Lemma, the following approximaiton error can be proved: if $u \in H^s(\Omega)$ is the solution of (2) with $f \in H^q(\Omega)$ ($q \geq 0$) and u_δ is the solution of the SEM-NI problem (7), then (see [5, 7, 8])

$$\|u - u_h\|_{H^r(\Omega)} \leq c \left(h^{\min(s,p+1)-r} p^{r-s} \|u\|_{H^s(\Omega)} + h^{\min(q,p+1)} p^{-q} \|f\|_{H^q(\Omega)} \right) \tag{9}$$
$$0 \leq r \leq 1, \quad s > d/2,$$

where $c = c(s, q, \Omega)$ is independent of both h and p. A key ingredient to prove (9) is the following interpolation error estimate ([5, 7, 8])

$$\|u - \mathcal{I}_\delta u\|_{H^r(\Omega)} \leq c h^{\min(s,p+1)-r} p^{r-s} \|u\|_{H^s(\Omega)} \qquad 0 \leq r \leq 1, \quad s > d/2, \tag{10}$$

where $\mathcal{I}_\delta : C^0(\Omega) \to X_\delta$ is the Lagrange interpolation operator at the LGL nodes.

If f is integrated exactly by the LGL quadrature formulas, the convergence estimate (9) simplifies as follows

$$\|u - u_h\|_{H^r(\Omega)} \leq c h^{\min(s,p+1)-r} p^{r-s} \|u\|_{H^s(\Omega)} \quad 0 \leq r \leq 1, \quad s > r, \tag{11}$$

If, in particular, $s > p + 1$ and $r = 1$, (11) becomes

$$\|u - u_h\|_{H^1(\Omega)} \leq c \left(\frac{h}{p} \right)^p \frac{1}{p^{s-p-1}} \|u\|_{H^s(\Omega)}. \tag{12}$$

We can express (12) in terms of the total number of degrees of freedom $N = (np + 1)^d \sim \left(\frac{p}{h} \right)^d$ (in view of the uniformity of the mesh) as follows

$$\|u - u_h\|_{H^1(\Omega)} \leq c N^{-p/d} \frac{1}{p^{s-p-1}} \|u\|_{H^s(\Omega)}. \tag{13}$$

Algebraic form forse scambiare come ordine *algebraic form* e *error estimate*

In order to represent the discrete solution u_δ, the nodal Lagrange basis functions $\varphi_i(\mathbf{x})$ (for $i = 1, \ldots, N$) defined over the set of LGL quadrature nodes are used, thus we have

$$u_\delta(\mathbf{x}) = \sum_{i=1}^{N} u_i \varphi_i(\mathbf{x}). \tag{14}$$

4

The SEM-NI stiffness matrix is defined by

$$(K_{SEM})_{ij} = a_\delta(\varphi_j, \varphi_i), \qquad i, j = 1, \ldots, N, \tag{15}$$

while the SEM-NI mass matrix by

$$(M_{SEM})_{ij} = (\varphi_j, \varphi_i)_\delta, \qquad i, j = 1, \ldots, N. \tag{16}$$

Thanks to the fact that the interpolation nodes coincide with the quadrature nodes, and noticing that the Lagrange basis functions are orthogonal with respect to the discrete inner product $(\cdot, \cdot)_\delta$, the SEM-NI mass matrix M_{SEM} is diagonal.

Let N^0 denote the number of degrees of freedom internal to Ω (we reorder all the mesh nodes so that the first N^0 are the internal ones), then we set $\mathbf{u}_{SEM} = [u_i]_{i=1}^{N^0}$ and $\mathbf{f}_{SEM} = [f(\mathbf{x}_i)]_{i=1}^{N^0}$. The algebraic form of (7) reads:

$$K_{SEM}\mathbf{u}_{SEM} = M_{SEM}\mathbf{f}_{SEM}, \tag{17}$$

where we understand that both K_{SEM} and M_{SEM} are restricted to the rows $i = 1, \ldots, N^0$ and the columns $j = 1, \ldots, N^0$.

The equivalent system

$$(M_{SEM})^{-1}K_{SEM}\mathbf{u}_{SEM} = \mathbf{f}_{SEM} \tag{18}$$

represents instead the algebraic counterpart of the *collocation* approximation to problem (1) at the LGL quadrature nodes (see [7]).

Both M_{SEM} and K_{SEM} are symmetric positive definite (s.p.d.) matrices. $(M_{SEM})^{-1}K_{SEM}$ is no longer symmetric, however it is similar to (and therefore share the same eigenvalues of) the s.p.d. matrix $(M_{SEM})^{-1/2}K_{SEM}(M_{SEM})^{-1/2}$.

2.2 Discretization by Isogeometric Analysis (IGA)

B-spline

Let $Z = \{0 = \zeta_0, \zeta_1, \ldots, \zeta_{n-1}, \zeta_n = 1\}$ be the set of $(n + 1)$ distinct knots in the one-dimensional patch $[0, 1]$ and, given two positive integers p and k with $0 \le k \le p - 1$, let

$$\Xi^{(k)} = \{\xi_1, \xi_2, \ldots, \xi_q\} = \{\underbrace{\zeta_0, \ldots, \zeta_0}_{p+1}, \underbrace{\zeta_1, \ldots, \zeta_1}_{p-k}, \ldots, \underbrace{\zeta_{n-1}, \ldots, \zeta_{n-1}}_{p-k}, \underbrace{\zeta_n, \ldots, \zeta_n}_{p+1}\} \tag{19}$$

be the $p-$open knot (ordered) vector with a fixed number of repetitions and with $q = (p - k)(n - 1) + 2p + 2$. The two extreme knots are repeated exactly $p + 1$ times, while the internal knots can be repeated at most p times. Then, after setting

$$B_{i,0}(\xi) = \begin{cases} 1 & \text{if } \xi_i \le \xi < \xi_{i+1} \\ 0 & \text{otherwise,} \end{cases} \tag{20}$$

we define the B-splines basis functions of local degree $p \geq 1$ and global regularity C^k by the Cox-de Boor recursion formula as follows ([14]):

$$B_{i,p}(\xi) = \frac{\xi - \xi_i}{\xi_{i+p} - \xi_i} B_{i,p-1}(\xi) + \frac{\xi_{i+p+1} - \xi}{\xi_{i+p+1} - \xi_{i+1}} B_{i+1,p-1}(\xi). \tag{21}$$

The functions $B_{i,p}$ intrinsically depend on the knots ξ_i as well as on the regularity k. In order to stay in compliance with the existing literature, we understand the dependence on k.

When p, n, and k are fixed, the number of linear independent B-splines $B_{i,p}$ is $n_b = (n-1)(p-k) + (p+1)$.

We will consider the two extreme values for k. When $k = 0$, the B-splines are only globally C^0 and we use the notation IGA-C^0 to identify this situation.

When $k = p - 1$, the B-splines are globally C^{p-1} and we write IGA-C^{p-1} to identify this case.

The d-times tensor product of the set Z induces a cartesian grid in the parametric domain $\Omega = (0,1)^d$. If we assume that the knots ζ_i are equispaced, the mesh size is $h = 1/n$.

When the geometric dimension d of the computational domain is greater than 1, we tensorize the set $\Xi^{(k)}$ and the B-splines functions. Then, for any $\mathbf{x} = (x_1, \ldots, x_d) \in \Omega$, let

$$\psi_{i,p}(\mathbf{x}) = B_{i_1,p}(x_1) \cdots B_{i_d,p}(x_d) \tag{22}$$

be the generic multivariate B-spline function, with $i = 1, \ldots, N_b = n_b^d$.

Formulation
Let us set

$$S_\delta^{(k)} = span\{\psi_{i,p}, \ i = 1, \ldots, N_b\} \tag{23}$$

and

$$V_\delta^{(k)} = V \cap S_\delta^{(k)}. \tag{24}$$

As for SEM, δ is an abridged notation now accounting for the number of distinct knots $(n+1)$ and the local polynomial degree p.

If, in particular, the partition $\mathcal{T}_h$ induced by the knot vector Z^d is the same for both SEM and IGA, the finite dimensional space $S_\delta^{(0)}$ of IGA-C^0 coincides with the finite dimensional space X_δ of SEM (see (3)) and then $V_\delta^{(0)} = V_\delta$.

The IGA-$C^{(k)}$ approximation of (2) reads: look for $u_{k,\delta} \in V_\delta^{(k)}$ such that

$$a(u_{k,\delta}, v_\delta) = \mathcal{F}(v_\delta) \qquad \forall v_\delta \in V_\delta^{(k)}. \tag{25}$$

Algebraic form
The discrete solution $u_{k,\delta}$ is expanded with respect to the B-spline basis functions, i.e.

$$u_{k,\delta}(\mathbf{x}) = \sum_{i=1}^{N_b} \hat{u}_{k,i} \psi_{i,p}(\mathbf{x}). \tag{26}$$

6

The IGA-$C^{(k)}$ stiffness matrix is defined by

$$(K_k)_{ij} = a(\psi_{j,p}, \psi_{i,p}), \qquad i,j = 1,\dots,N_b, \tag{27}$$

while the IGA-$C^{(k)}$ mass matrix is defined by

$$(M_k)_{ij} = (\psi_{j,p}, \psi_{i,p})_{L^2(\Omega)}, \qquad i,j = 1,\dots,N_b. \tag{28}$$

Both M_k and K_k are symmetric positive definite (s.p.d.) matrices.

To write the algebraic counterpart of (7) we denote by N^0 the number of degrees of freedom internal to Ω (we reorder all the mesh nodes so that the first N^0 are the internal ones in lexicographic order (non so se sia essenziale dirlo)), then we set $\mathbf{u}_k = [\hat{u}_{k,i}]_{i=1}^{N^0}$ and $\mathbf{f}_k = [\hat{f}_{k,i}]_{i=1}^{N^0}$ with $\hat{f}_{k,i} = (f, \psi_{i,p})_{L^2(\Omega)}$.

The algebraic form of (7) reads: look for the solution $\mathbf{u}_k$ of

$$K_k \mathbf{u}_k = \mathbf{f}_k, \tag{29}$$

where we understand that K_k is restricted to the rows $i = 1,\dots,N^0$ and the columns $j = 1,\dots,N^0$.

Error estimates

Under the assumption that the partition defined by the knot vector Z is locally quasi uniform, that is, there exists a constant $\theta \geq 1$ such that the mesh sizes $h_i = \zeta_{i+1} - \zeta_i$ satisfy the relation $\theta^{-1} \leq h_i/h_{i+1} \leq \theta$ for $i = 0,\dots,n-1$, in [10, Thm. 3.4] it is proved that there exists a positive constant $c = c(s,p,\theta)$ independent of $h = \max_i h_i$ such that

$$\|u - u_{k,\delta}\|_{H^1(\Omega)} \leq c h^{\min(s,p+1)} \|u\|_{H^s(\Omega)} \qquad \forall u \in H^s(\Omega). \tag{30}$$

This is an optimal convergence estimate for IGA with respect to h for all values of $k = 0,\dots,p-1$.

The convergence rate of IGA methods with respect to both p and k has been studied in [9] when $p \geq 2k+1$. We warn the reader that in the present paper the parameter k is used to indentify the C^k regularity of the B-spline basis functions (and then of the IGA solution). Differently, in the paper [9], the parameter k stands for the Sobolev regularity of the IGA solution. In order to avoid misunderstandings, we denote by k_b the index k used in [9], it holds $k_b = k+1$.

For any $k_b \geq 0$ integer, in [9] the authors introduce a projection operator $\hat{\pi}_{p,k_b} : H^{k_b}(\Lambda) \to \mathbb{P}_p(\Lambda)$, with $\Lambda = (-1,1)$ and $\mathbb{P}_p(\Lambda)$ the space of retriction to Λ of polynomials of degree almost p, such that

$$(\hat{\pi}_{p,k_b} u)^{(j)}(\pm 1) = u^{(j)}(\pm 1), \qquad j = 0,\dots,k_b - 1. \tag{31}$$

$\hat{\pi}_{p,k_b}$ is not the orthogonal projection operator from $H^{k_b}(\Lambda)$ to $\mathbb{P}_p(\Lambda)$, nevertheless it is a projection operator that perserves the values of the function and of its derivatives up to order $k_b - 1$ at the end-points of Λ. Moreover, if $u : \Lambda \to \mathbb{R}$ with $u^{(k_b)} \in H^s(\Lambda)$, if $p \geq 2k_b - 1$ and $s \leq p - k_b + 1$, then for any $j = 0,\dots,k_b$ it holds ([9, Cor. 2])

$$\|u^{(j)} - (\hat{\pi}_{p,k_b} u)^{(j)}\|_{L^2(\Lambda)} \leq C \left(\frac{e}{2}\right)^{s+k_b-j} (p - k_b + 1)^{-(s+k_b-j)} |u^{(k_b)}|_{H^s(\Lambda)}. \tag{32}$$

By introducing the linear continuous mappings $T_i : \Lambda \to I_i = (\zeta_i, \zeta_{i+1})$, for $i = 0, \ldots, n-1$ (such that $T_i(\xi) = \xi(\xi_{i+1} - \xi_i)/2 + (\xi_{i+1} - \xi_i)/2$), we can define the global projection operator $\pi_{p,k_b} : H^{k_b}(0,1) \to S_\delta^{(k_b-1)}$ by the relations

$$(\pi_{p,k_b} u) \circ T_i = \hat{\pi}_{p,k_b}(u \circ T_i), \qquad i = 1, \ldots, n-1. \tag{33}$$

For any $u \in H^{k_b}(0,1)$, $\pi_{p,k_b} u$ preserves the values of u and of all its derivatives up to order $k_b - 1$ at the knots ζ_i, for $i = 0, \ldots, n$.

If the partition induced by the knot vector Z is uniform of size h, then ([9, Thm. 2])

$$\|u - \pi_{p,k_b} u\|_{H^j(0,1)} \leq C h^{\sigma - j}(p - k_b + 1)^{-(\sigma - j)} \|u\|_{H^\sigma(0,1)} \qquad \forall u \in H^\sigma(0,1), \tag{34}$$

for any $j = 0, \ldots, k_b$, for $k_b \leq \sigma \leq p+1$, and $p \geq 2k_b - 1$, with C independent of σ, j, h, p and k_b.

Thus, recalling that $k_b = k+1$ and thanks to (34) and to the Céa's lemma, it holds

$$\|u - u_{k,\delta}\|_{H^j(0,1)} \leq C h^{\sigma - j}(p - k)^{-(\sigma - j)} \|u\|_{H^\sigma(0,1)} \tag{35}$$

for $0 \leq j \leq k+1 \leq \sigma \leq p+1$ and $p \geq 2k+1$, i.e. the convergence of IGA is optimal also w.r.t. to p and k.

In the next Theorem we extend the convergence estimate (35) to any $\sigma \geq k+1$ by applying a result of [6]. In this way we can remove the upper bound $\sigma \leq p+1$ (that is essential in proving (32)).

Theorem 1 *Let $d = 1$, $p \geq 1$ and $k \geq 0$ be two integers with $p \geq 2k+1$, and let $u_{k,\delta} \in V_\delta^{(k)}$ be the solution of (25). Let the solution u of (2) belong to $H^s(\Omega)$ with $s \geq k+1$. Then, if the partition induced by the knot vector Z is uniform of size h, for any real numbers r and s with $0 \leq r \leq k+1 \leq s$, it holds*

$$\|u - u_{k,\delta}\|_{H^r(0,1)} \leq C h^{s-r}(p - k)^{-(s-r)} \|u\|_{H^s(0,1)}, \tag{36}$$

with C independent of both h and p.

Proof. The proof strictly follows the arguments developed in [6, Sect.6], however we report it for reader convenience.

Let $k_b \geq 0$ and $p \geq 2k_b - 1$ be two integers. First, we consider the orthogonal projection operator $\pi_p^{k_b,0} : H^s(\Lambda) \cap H_0^{k_b}(\Lambda) \to \mathbb{P}_p^{k_b,0}(\Lambda) = \mathbb{P}_p(\Lambda) \cap H_0^{k_b}(\Lambda)$, that satisfies (see the proof of Theorem 6.2 of [6])

$$\|u - \pi_p^{k_b,0} u\|_{H^r(\Lambda)} \leq c(p - k_b)^{r-s} \|u\|_{H^s(\Lambda)} \qquad \forall u \in H^s(\Lambda) \cap H_0^{k_b}(\Lambda), \tag{37}$$

with $0 \leq r \leq k_b \leq s$ and c independent of p.

Then, we introduce a set of polynomials $\chi_{k_b,\ell}$, $0 \leq \ell \leq k_b - 1$ such that $\chi_{k_b,\ell} \in \mathbb{P}_{2k_b - 1}(\Lambda)$ is the unique polynomial satisfying

$$\chi_{k_b,\ell}^{(\ell)}(-1) = 1, \qquad \chi_{k_b,\ell}^{(m)}(-1) = 0, \quad 0 \leq m \leq k_b - 1, \ m \neq \ell,$$
$$\chi_{k_b,\ell}(1) = \chi'_{k_b,\ell}(1) = \cdots = \chi_{k_b,\ell}^{(k_b-1)}(1) = 0,$$

and we define the polynomial

$$\chi_{k_b}(\zeta) = \sum_{\ell=0}^{k_b-1} u^{(\ell)}(-1)\chi_{k_b,\ell}(\zeta) + \sum_{\ell=0}^{k_b-1}(-1)^\ell u^{(\ell)}(1)\chi_{k_b,\ell}(-\zeta) \tag{38}$$

and the function $\tilde{u}_{k_b} = u - \chi_{k_b} \in H_0^{k_b}(\Lambda)$.

The projection operator $\widetilde{\pi}_p^{k_b} : H^{k_b}(\Lambda) \to \mathbb{P}_p(\Lambda)$ is defined for any $k_b \geq 1$ and $p \geq 2k_b - 1$ by

$$\widetilde{\pi}_p^{k_b} u = \pi_p^{k_b,0} u + \chi_{k_b}. \tag{39}$$

It perserves the values of the function and of its derivatives of order up to $k_b - 1$ at the end-points of Λ. Thanks to (39) it holds

$$u - \widetilde{\pi}_p^{k_b} u = \tilde{u}_{k_b} - \pi_p^{k_b,0}\tilde{u}_{k_b}, \tag{40}$$

thus, thanks to (37) and the fact that the map $u \mapsto \tilde{u}_{k_b}$ is continuous in $H^s(\Lambda)$ (see [6, formula (6.19)]), we have

$$\|u - \widetilde{\pi}_p^{k_b} u\|_{H^r(\Lambda)} \leq c(p - k_b)^{r-s}\|u\|_{H^s(\Lambda)} \qquad \forall u \in H^s(\Lambda) \tag{41}$$

for any integer $k_b \geq 1$ and $p \geq 2k_b - 1$ and for any real numbers r and s such that $0 \leq r \leq k_b \leq s$, with c independent of both p.

By using the linear mappings T_i introduced above and starting from $\widetilde{\pi}_p^{k_b}$ we define a global projection operator $\pi_p^{k_b} : H^{k_b}(0,1) \to \mathcal{S}_\delta^{(k_b-1)}$ that preserves the values of u and its derivatives up to order $k_b - 1$ at the end-points of each interval I_i. By using the uniform distribution of the knot vector Z and by standard scaling arguments it holds

$$\|u - \pi_p^{k_b} u\|_{H^r(0,1)} \leq Ch^{\min(p+1,s)-r}(p - k_b)^{r-s}\|u\|_{H^s(0,1)} \qquad \forall u \in H^s(0,1), \tag{42}$$

with $0 \leq r \leq k_b \leq s$ and c independent of both h and p.

By setting $k = k_b - 1$, noticing that $\frac{1}{2} \leq \frac{p-k}{p-k+1} \leq 1$ for any $p \geq 2k + 1$ and thanks to Céa's Lemma, the thesis follows. $\qquad\square$

The analysis for $p \geq 2k + 1$ is still open [10, Remark 4.18].

The analysis for the case $d = 2$ is developed in [6, Sect. 7] and in [9]. In particular, referring to [9], if $Q = \Lambda^2$, if the partition induced by the knot vector $Z \times Z$ is uniform, and if the same p and k are used along the two directions, then ([9, Cor. 8])

$$\|u - u_{k,\delta}\|_{H^\ell(Q)} \leq ch^{\sigma-\ell}(p - k)^{-(\sigma-\ell)}\|u\|_{H^\sigma(Q)} \qquad \forall u \in H^\sigma(Q), \tag{43}$$

for any $0 \leq \ell \leq k + 1$, provided that $2k + 2 \leq s \leq p + 1$. Moreover, the positive constant c is independent of s, ℓ, h, p and k.

When $d = 3$, by assuming again that p and k are the same along all directions, the more restrictive condition $3k + 3 \leq \sigma \leq p + 1$ should be assumed to prove an analogous estimate (see [9, Remark 1, pag. 300] and [6, Remark 7.1]).

3 Convergence rate: numerical tests

We consider problem (1) with $d = 3$ and choose the right hand side f so that the exact solution is

$$u(x) = \sin(4\pi xyz)\sin(4\pi(x-1)(y-1)(z-1)). \qquad (44)$$

Then we solve it by IGA-C^0, IGA-C^{p-1} and SEM on a set of uniform grids of size $h \in [1/16, 1/2]$ and with local polynomial degree $p = 1, \ldots, 8$. We recall that, if n is the number of elements along each direction, then $h = 1/n$ for all the methods.

We omit here to show numerical results for $d = 1$ and $d = 2$ since the methods behave similarly to the case $d = 3$.

Error versus h and p

In Figure 1 we show the H^1-norm (at left) and the L^2-norm (at right) of the errors between the numerical solutions (obtained by one of the three methods IGA-C^0, IGA-C^{p-1} and SEM) and the exact solution (44), versus the polynomial degree p, with h fixed. The H^1-norm of the IGA-C^0 and SEM errors coincide: as we can see in both pictures of Figure 1 the markers (that represent the errors for IGA-C^0) are overlapped with the continuous lines (that represent the errors for SEM). The errors of IGA-C^{p-1} (dashed lines) have the slowest decay rate.

The exact solution we are considering is analytical, thus (in view of the estimates (11) and (36), suitable extended to the acse $d = 3$) the errors of IGA-C^0 and SEM decay with respect to p faster than any algebraic power of p, i.e., exponentially with respect to p.

The errors of IGA-C^{p-1} decay more slowly than the others, even if the exponential behavior seems to occur also in this case. sembra in contraddizione con quanto detto sopra

~~The L^2-norm of the error for IGA-C^0 are slightly lower than the corresponding SEM errors. The L^2-norm of the error for SEM is bounded from below by the stopping tolerance $\epsilon = 10^{-12}$ of the Bi-CGstab method called to solve the algebraic linear system.~~ Ho rilanciato con $\epsilon = 10^{-16}$, ma l'errore diminuisce di molto poco, si vede che è l'effetto dell'arrotondamento in genere.

In Figure 2 we show the H^1-norm (top) and the L^2-norm (bottom) of the errors between the numerical solutions and the exact solution (44), versus the mesh size h, when p is fixed. In Table 1 we show the convergence orders w.r.t. h, that we have estimated starting from the errors reported in Fig. 2. The errors of IGA-C^0 and SEM obey the estimates (11) and (30) with respect to h, while the errors of IGA-C^{p-1} exhibit superconvergence w.r.t. h.

Error versus dof

The total number of degrees of freedom (dof) of the discretization is reported below:

	IGA-C^0	IGA-C^{p-1}	SEM
dof	$(np+1)^d$	$(p+n)^d$	$(np+1)^d$.

In Figure 3 the H^1-norm (at left) and the L^2-norm (at right) of the errors are plotted versus $dof = dof(p)$, with h fixed.
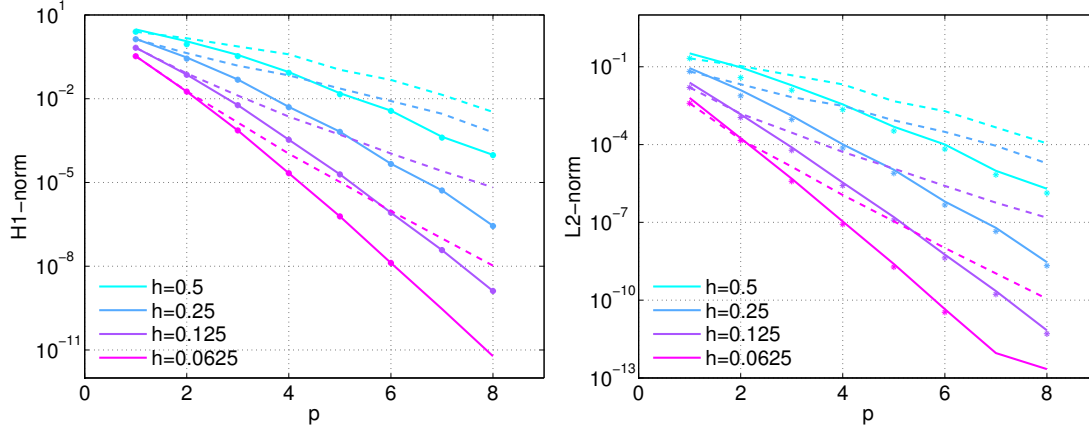
Figure 1: H^1-norm (left) and L^2-norm (right) of the errors versus the polynomial degree p. Markers refer to IGA-C^0 solution, dashed lines refer to IGA-C^{p-1} solution, while the continuous lines refer to SEM solution. The color identifies the mesh size h

Table 1: Convergence orders w.r.t. h

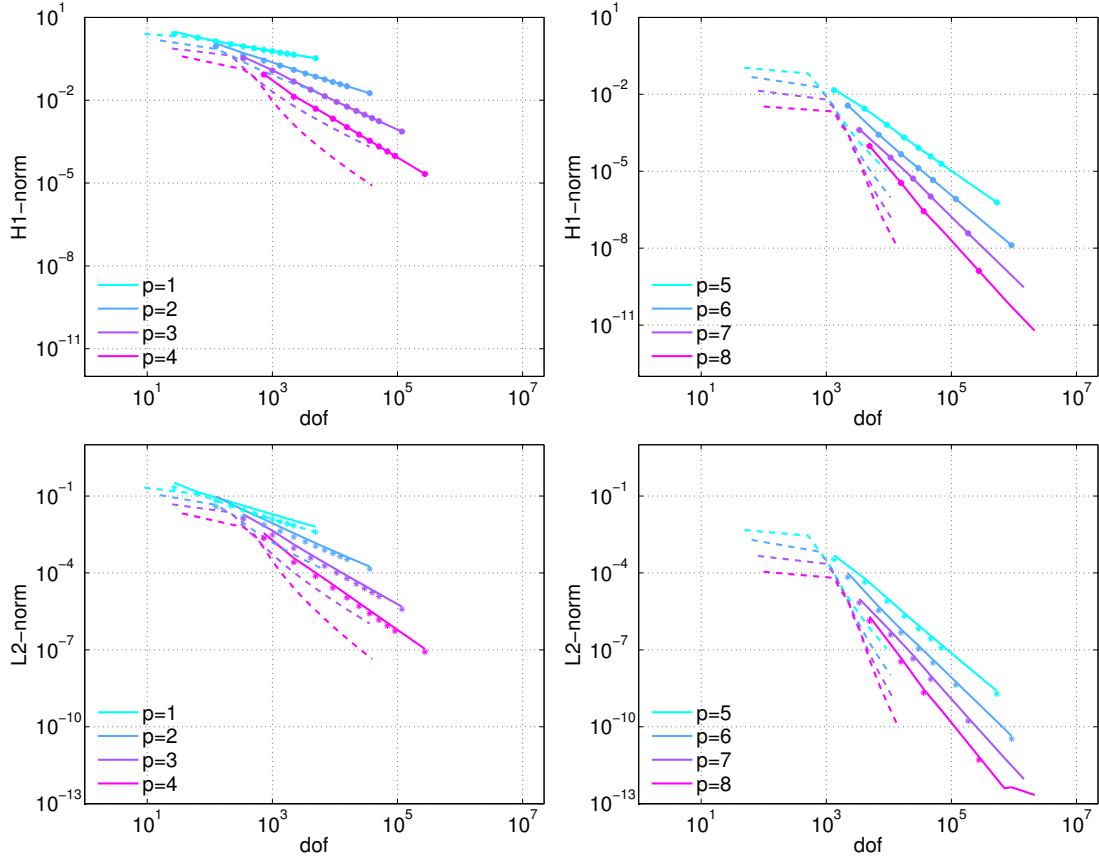| p	H^1-norm			L^2-norm		
	IGA-C^0	IGA-C^{p-1}	SEM	IGA-C^0	IGA-C^{p-1}	SEM
1	1.00	1.00	1.02	2.02	2.02	1.95
2	1.99	2.15	2.02	2.94	3.35	3.06
3	3.00	3.08	3.01	3.97	4.15	4.01
4	3.97	4.16	3.99	4.95	5.23	4.99
5	5.03	5.70	5.01	6.00	6.82	6.00
6	5.99	6.93	5.98	6.93	8.05	6.98
7	6.71	8.13	7.01	7.68	9.17	7.96
8	8.09	9.16	7.82	9.03	10.52	8.92
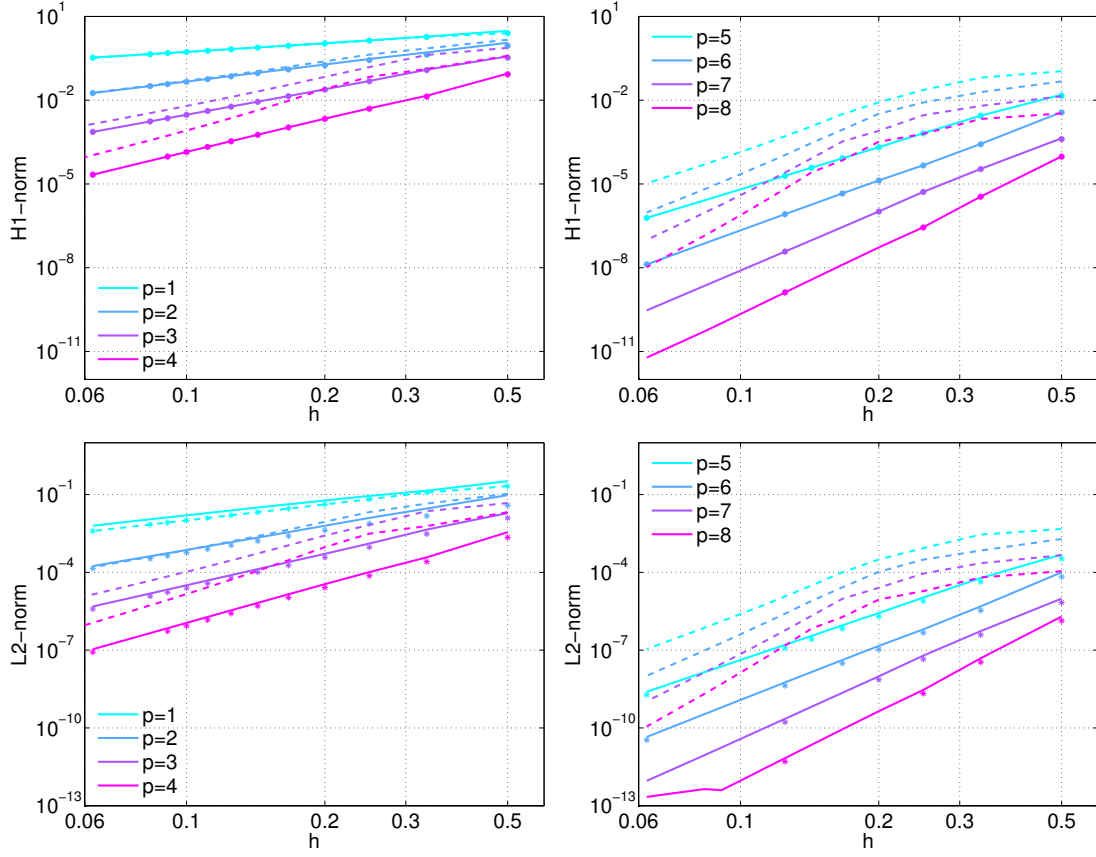
Figure 2: H^1-norm (top) and L^2-norm (bottom) of the errors versus the mesh size h. Markers refer to IGA-C^0 solution, dashed lines refer to IGA-C^{p-1} solution, while continuous lines refer to SEM solution. The color identifies the polynomial degree p

12
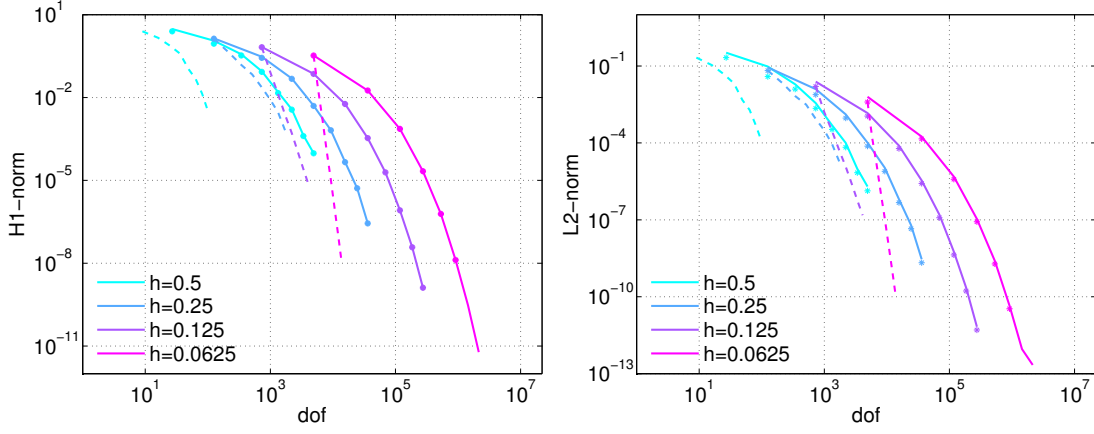
Figure 3: H^1−norm (left) and L^2−norm (right) of the errors versus $dof = dof(p)$. Markers refer to IGA-C^0 solution, dashed lines refer to IGA-C^{p-1} solution, while the continuous lines refer to SEM solution. The color identifies the mesh size h

Similarly, in Figure 4 we report the H^1-norm (top) and the L^2-norm (bottom) of the errors versus $dof = dof(h)$, with p fixed.

IGA-C^{p-1} provides the minimum error (compared with IGA-C^0 and SEM) for a fixed dof.

Matrix sparsisty pattern

Nevertheless, dof is not the unique reference parameter that we have to take into account in measuring the efficiency of a method.

As a matter of fact, other important ingredients that get into the game in solving the linear systems (17) and (29), especially when $d = 3$, are the sparsity pattern of the stiffness matrix and its *number of nonzero entries (nnz)*. The latter is a measure not only of the memory space required to storage the matrix, but also of the computational complexity of the algebraic solver.

The numerical results shown in this Sections have been produced using an Intel(R) Core(TM) i7-4790 CPU @ 3.60GHz with 4 Cores and 16GB of RAM. When $d = 3$, starting from moderate values of p (e.g. $p = 4$) and moderate values of $n = 1/h$ (e.g. $n = 8$) the direct solution of linear systems (17) and (29) is prohibitive, unless one has highly powerfull architectures available. This is due to the fill-in occuring during the eliminitation process.

As a consequence a preconditioned iterative method, like, e.g., Krylov ones, is in order. To solve the linear systems we called the Bi-GCStab method [19], preconditioned by an incomplete LU factorization. On this machine, the iterative numerical solution of the linear system of IGA-C^0 becomes prohibitive for $p > 4$ and $n > 7$.

Even if both the IGA and SEM stiffness matrices are symmetric and positive definite, we have called the Bi-GCStab instead of the Conjugate Gradient method. As a matter

Figure 4: H^1−norm (top) and L^2−norm (bottom) of the errors versus $dof = dof(h)$. Markers refer to IGA-C^0 solution, dashed lines refer to IGA-C^{p-1} solution, while the continuous lines refer to SEM solution. The color identifies the polynomial degree p

14
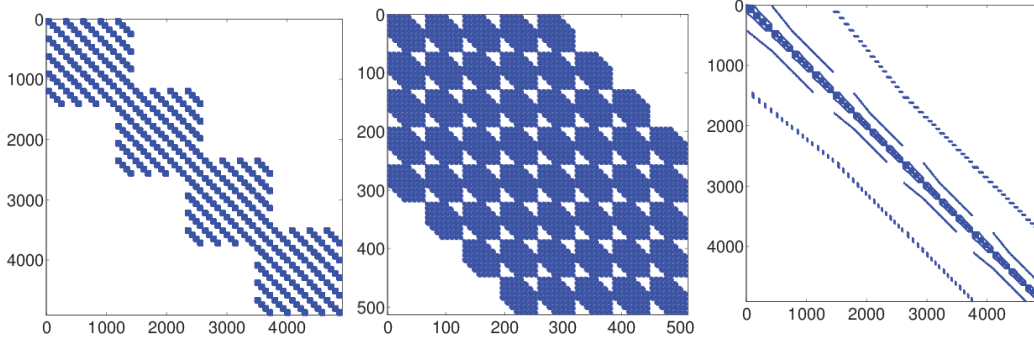
Figure 5: Pattern of the stiffness matrix of IGA-C^0 (left), IGA-C^{p-1} (center), and SEM (right). dof is 4193 for both IGA-C^0 and SEM, while it is 512 for IGA-C^{p-1}. nnz is 911599 for IGA-C^0, 140604 for IGA-C^{p-1}, and 46575 for SEM

of fact, since the condition number of the IGA stiffness matrices heavily grows with p (see the next sections), the symmetric incomplete Cholesky factorization often broke for having tried to compute the square root of non-positive values.

At each iteration of the Krylov method, one has to compute matrix-vector products and solve auxiliary linear systems related to the preconditioner. We neglect here the analysis of the costs associated with the preconditioner, that goes out the porpuses of the present work.

The computational costs of one matrix-vector products (mvp in brief) is about $2\,nnz$ floating point operations, thus it is meaningful to measure the approximation errors also in terms of this parameter.

First of all we notice that nnz can be written in terms of $n = 1/h$ and p as (c is a positive constant independent of n and p that can be different method by method)

	IGA-C^0	IGA-C^{p-1}	SEM
nnz	$c\,p^{2d}n^d$	$c\,(p^{2d} + p^d n^d)$	$c\,d\,p^{d+1}n^d.$

While the dependence on n (and then on h) is the same for all the three methods, the dependence on p strongly varies method by method.

We notice that, in the case of SEM, nnz is independent of the fact that quadrature formulas are used to approximate integrals. The same sparsity pattern would be obtained if one uses exact integration instead of the numerical one.

In Fig. 5 the pattern of the stiffness matrix of all the three methods are shown, for the case $p = 4$ and $n = 4$, when $d = 3$.

Then, in Fig. 6 we show the H^1-norm of the error versus $nnz = nnz(p)$ with h fixed (top) and versus $nnz = nnz(h)$ with p fixed (bottom).

In both cases, SEM is the method (among the three) that provides the minimum errors for nnz fixed.

15
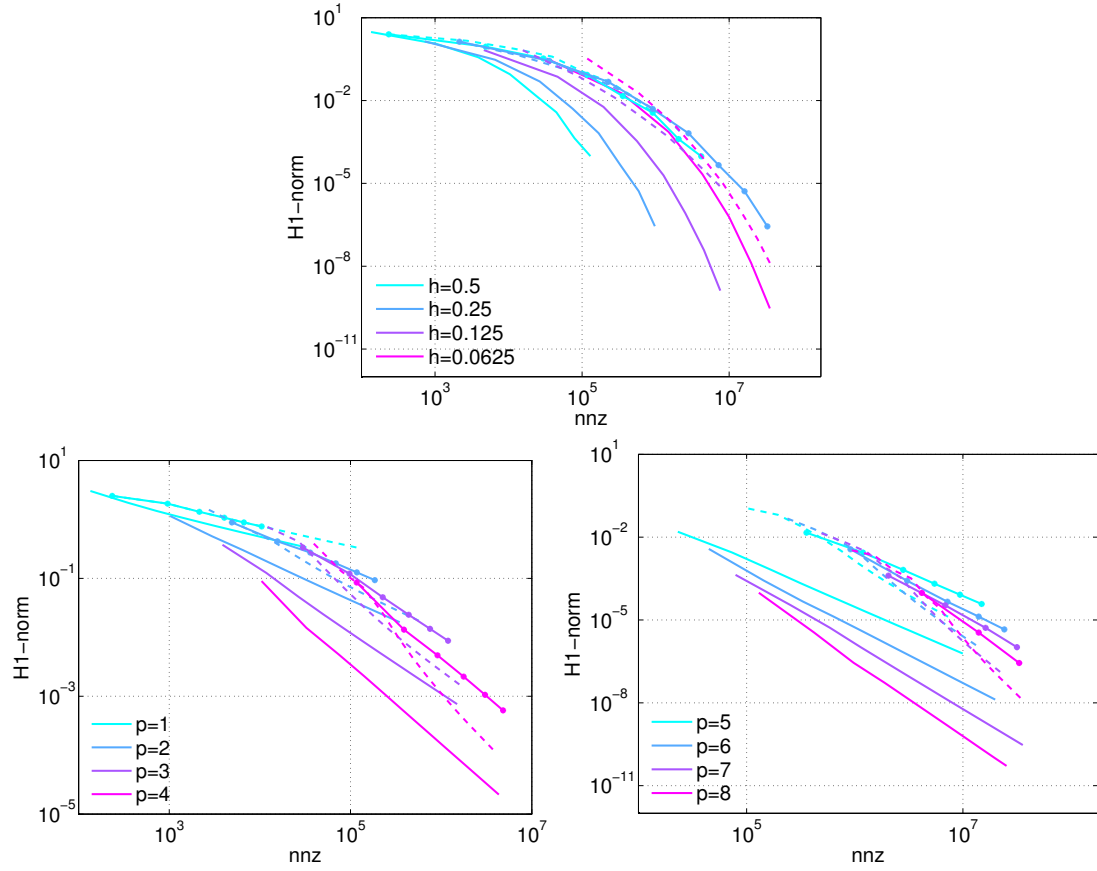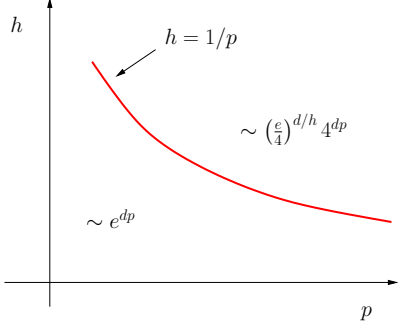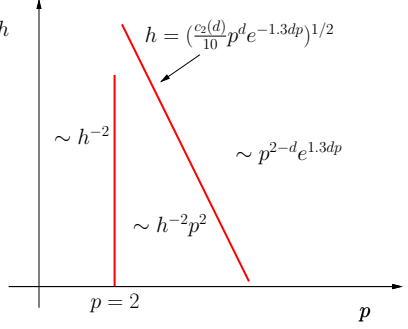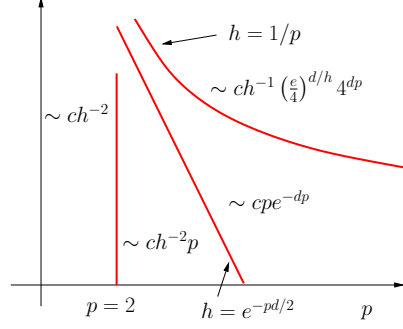
Figure 6: H^1-norm of the error versus $nnz = nnz(p)$ (top) and versus $nnz = nnz(h)$ (bottom). Markers refer to IGA-C^0 solution, dashed lines refer to IGA-C^{p-1} solution, while the continuous lines refer to SEM solution. The color identifies the mesh size h

Table 2: Condition numbers of mass and stiffness matrices

	SEM	IGA-C^0	IGA-C^{p-1}
$\mathcal{K}(M)$	p^d	$p^{-d/2}4^{pd}$	h-vs-p plot: curve labelled $h = 1/p$; $\sim \left(\frac{e}{4}\right)^{d/h} 4^{dp}$; $\sim e^{dp}$
$\mathcal{K}(K)$	$h^{-2}p^3$	h-vs-p plot: line labelled $h = (\frac{c_2(d)}{10}p^d e^{-1.3dp})^{1/2}$; $\sim h^{-2}$; $\sim p^{2-d}e^{1.3dp}$; $\sim h^{-2}p^2$; $p = 2$	h-vs-p plot: curve labelled $h = 1/p$; $\sim ch^{-2}$; $\sim ch^{-1}\left(\frac{e}{4}\right)^{d/h} 4^{dp}$; $\sim cpe^{-dp}$; $\sim ch^{-2}p$; $p = 2$; $h = e^{-pd/2}$

4   Extreme eigenvalues and condition number

In this section we summarize the main results concerning the spectral properties of SEM and IGA arrays. Because of their importance for the convergence rate of iterative methods, we specifically highlight the behaviour of the extreme eigenvalues (and the corresponding spectral condition number) of mass matrices and stiffness matrices.

For any matrix A symmetric positive definite (or similar to a symmetric positive definite matrix) let $\lambda_{min}(A)$ and $\lambda_{max}(A)$ denote its minimum and maximum (real) eigenvalues, respectively. The *spectral condition number* of A is defined as

$$\mathcal{K}(A) = \frac{\lambda_{max}(A)}{\lambda_{min}(A)}. \tag{45}$$

The extreme eigenvalues of the SEM mass and stiffness matrices behave as follows

([5, 15, 7, 8]):

$$\lambda_{min}(M_{SEM}) \quad \sim \quad c_1 h^d p^{-2d} \tag{46}$$
$$\lambda_{max}(M_{SEM}) \quad \sim \quad c_2 h^d p^{-d} \tag{47}$$
$$\lambda_{min}(K_{SEM}) \quad \sim \quad c_3(d) h^d p^{-d} \tag{48}$$
$$\lambda_{max}(K_{SEM}) \quad \sim \quad c_4(d) h^{d-2} p^{3-d} \tag{49}$$
$$\lambda_{min}((M_{SEM})^{-1}K_{SEM}) \quad \sim \quad c_5(d) \tag{50}$$
$$\lambda_{min}((M_{SEM})^{-1}K_{SEM}) \quad \sim \quad c_6(d) h^{-2} p^4. \tag{51}$$

The corresponding iterative condition numbers are, for $d = 1, 2, 3$:

$$\mathcal{K}(M_{SEM}) \quad \sim \quad p^d \tag{52}$$
$$\mathcal{K}(K_{SEM}) \quad \sim \quad p^3 h^{-2} \tag{53}$$
$$\mathcal{K}((M_{SEM})^{-1}K_{SEM}) \quad \sim \quad p^4 h^{-2}, \tag{54}$$

they are reported in Table 2.

Discorso generale sulle costanti: le lasciamo, le togliamo? Mettiamo una c generica per tutti, altrimenti sono veramente tante.

The eigenvalues and the condition number of IGA matrices have been studied in [12, 13].

In [12] it is proved for $d = 2$ that, independently of the k-regularity of the B-spline basis functions, it holds:

$$
\begin{aligned}
&\lambda_{min}(M_k) \sim c(p)h^2, \qquad \lambda_{min}(M_k) \geq c(h)p^{-4}16^{-p} \\
&\lambda_{max}(M_k) \sim c(p)h^2, \qquad \lambda_{max}(M_k) \sim c(h)p^{-2}, \\
&\mathcal{K}(M_k) \leq cp^2 16^p, \text{ with } c \text{ indep. of } h \text{ and } p, \\
&\lambda_{min}(K_k) \sim c(p)h^2, \\
&\lambda_{max}(K_k) \sim c, \text{ with } c \text{ indep. of } h \text{ and } p, \\
&\mathcal{K}(K_k) \leq c(h)p^8 16^p,
\end{aligned}
\tag{55}
$$

where M_k and K_k are the mass matrix and the stiffness matrix of IGA approximation for a generic $k = 0, \dots, p-1$.

In [13] the authors prove for $d = 1$, $p \geq 1$ and $n \geq 2$ that

$$
\begin{aligned}
&\lambda_{min}(M_{p-1}) \geq hc(p), \\
&\lambda_{min}(K_{p-1}) \geq \pi^2 hc(p).
\end{aligned}
\tag{56}
$$

Other estimates about the clustering of the eigenvalues of the matrix discretizing the advection-diffusion-reaction operator for $d = 1$ are proved in [13].

We have numerically computed the extreme eigenvalues of the mass and stiffness matrices for both IGA-C^0 and IGA-C^{p-1} using the function `eigs` of Matlab for different values of h and p, then we have estimated their behaviour w.r.t. both h and p.

4.1 IGA-C^0 mass matrix

If we denote with M_0 the mass matrix associated with IGA-C^0 approximation, our numerical results show that, for any value of $h > 0$ and $p \geq 1$, $\lambda_{min}(M_0)$ and $\lambda_{max}(M_0)$ behave as:

$$\lambda_{min}(M_0) \quad \sim \quad c(d)h^d p^{-d/2} 4^{-pd}, \tag{57}$$

$$\lambda_{max}(M_0) \quad \sim \quad \frac{1}{c(d)} h^d p^{-d}, \tag{58}$$

for $d = 1, 2, 3$. The constants $c(d) > 1$ are of the order of the unity: $c(1) \sim 1.2$, $c(2) \sim 1.2$ and $c(3) \sim 1.7$. Then

$$\mathcal{K}(M_0) \sim p^{-d/2} 4^{pd}. \tag{59}$$

In Figures 7 – 12 we show the computed eigenvalues (at left) and the r.h.s. of (57) – (58) w.r.t. h and p.

Va bene così? Vi sembrano chiare tutte queste figure sugli autovalori? Pensate sia meglio un altro tipo di grafica?
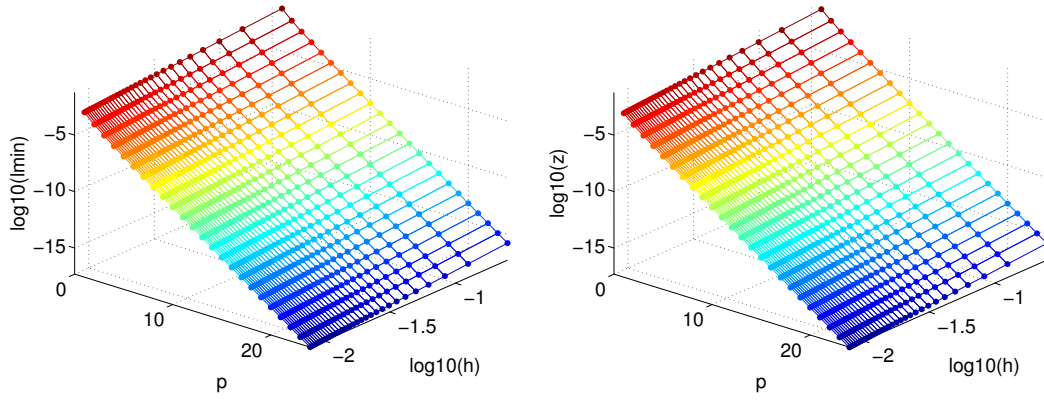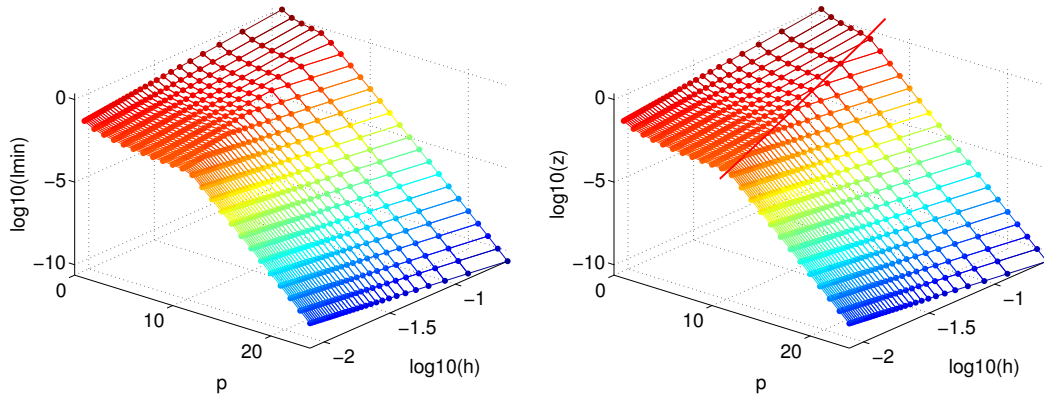

Figure 7: At left, the numerically computed values of $\lambda_{min}(M_0)$ for $d = 1$ and for different values of h and p. At right, the graphical representation of the r.h.s. of (57). $c(1) \simeq 1.2$
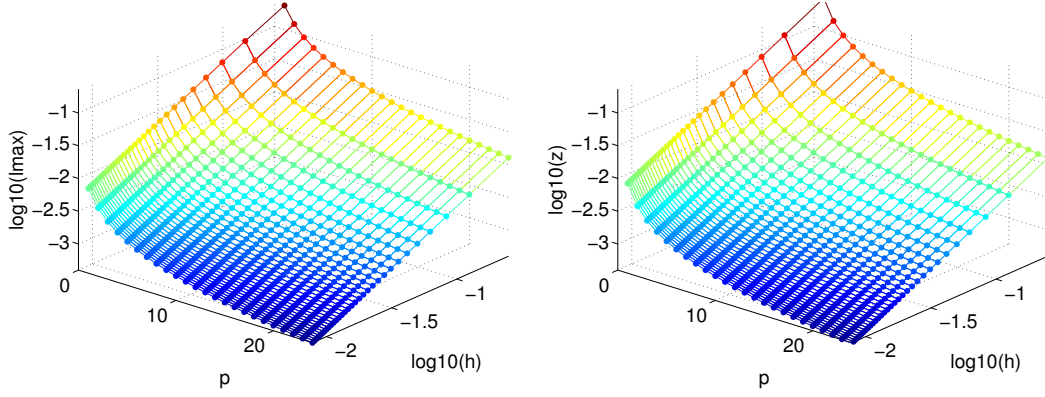
Figure 8: At left, the numerically computed values of $\lambda_{max}(M_0)$ for $d = 1$ and for different values of h and p. At right, the graphical representation of the r.h.s. of (58). $c(1) \simeq 1.2$
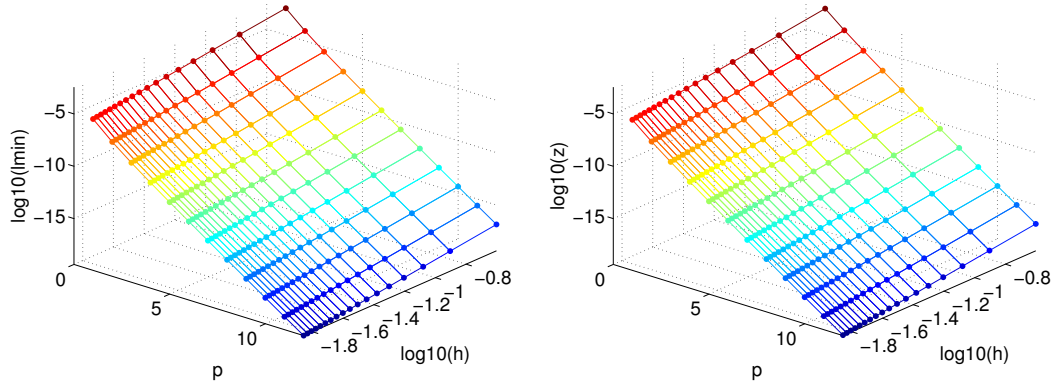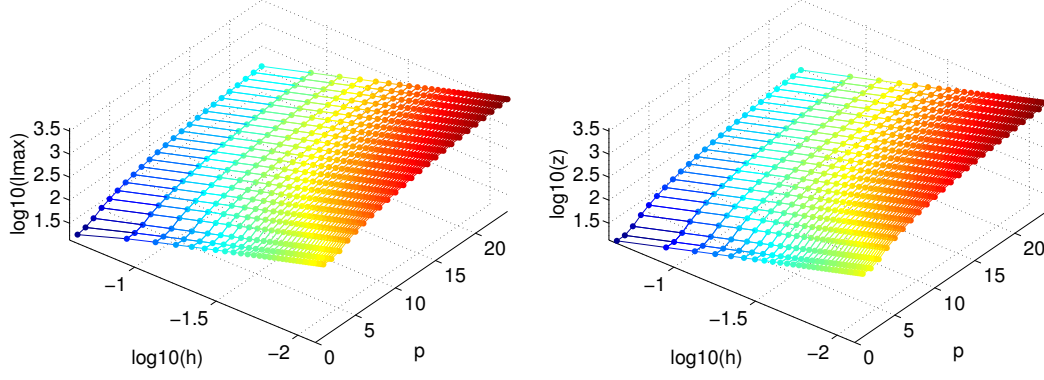

Figure 9: At left, the numerically computed values of $\lambda_{min}(M_0)$ for $d = 2$ and for different values of h and p. At right, the graphical representation of the r.h.s. of (57). $c(2) \simeq 1.2$
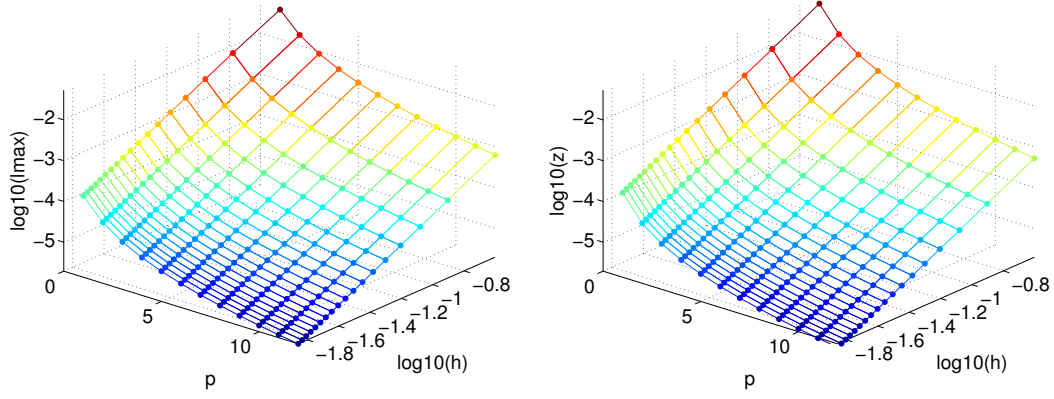
Figure 10: At left, the numerically computed values of $\lambda_{max}(M_0)$ for $d = 2$ and for different values of h and p. At right, the graphical representation of the r.h.s. of (58). $c(2) \simeq 1.2$
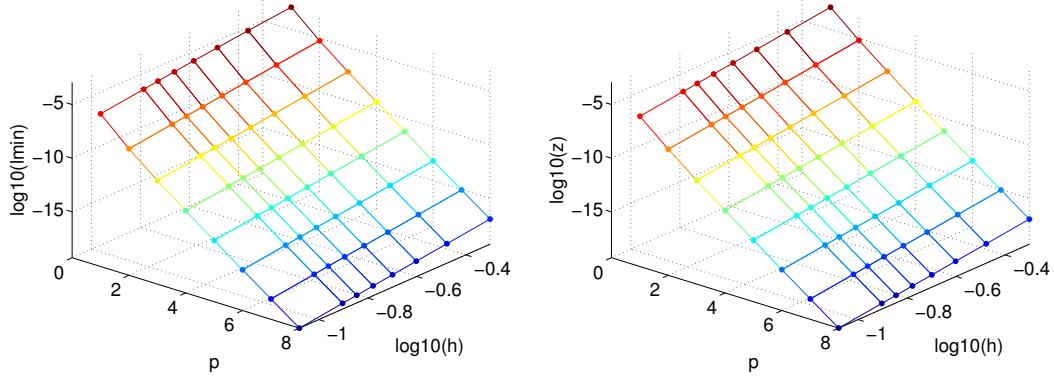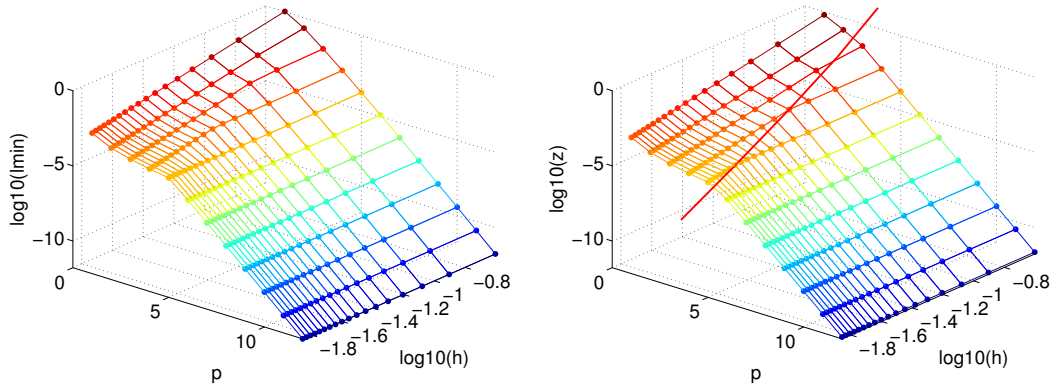

Figure 11: At left, the numerically computed values of $\lambda_{min}(M_0)$ for $d = 3$ and for different values of h and p. At right, the graphical representation of the r.h.s. of (57). $c(3) \simeq 1.7$
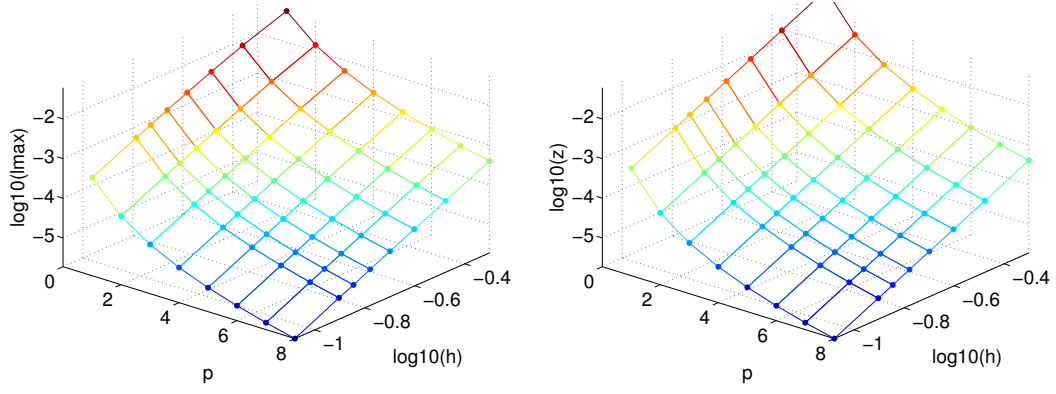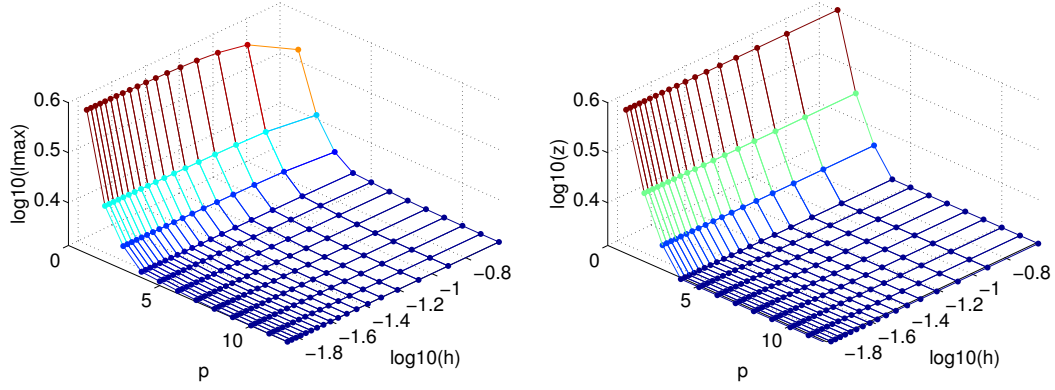
Figure 12: At left, the numerically computed values of $\lambda_{max}(M_0)$ for $d = 3$ and for different values of h and p. At right, the graphical representation of the r.h.s. of (58). $c(3) \simeq 1.7$

4.2 IGA-C^0 stiffness matrix

Denoting by K_0 the stiffness matric corresponding to the IGA-C^0 approximation, its computed extreme eigenvalues behave depending as follows (see also Fig. 13):

$$\lambda_{min}(K_0) \sim \begin{cases} c_1 h^d p^{-d} & \text{if } h \leq \left(\frac{c_2(d)}{c_1} p^d e^{-1.3dp}\right)^{1/2} \\ c_2(d) h^{d-2} e^{-1.3\,dp} & \text{otherwise} \end{cases} \tag{60}$$

$$\lambda_{max}(K_0) \sim \begin{cases} c_3 h^{d-2} p^{(1-d)/2} & \text{if } p \leq \overline{p}(d) \\ c_4 h^{d-2} p^{2-d} & \text{otherwise} \end{cases} \tag{61}$$

for any $d = 1, 2, 3$.

The behaviour of the condition number $\mathcal{K}(K_0)$ versus both h and p is shown in Fig. 14

Dite che è il caso di togliere la distinzione $p > < \overline{p}(d)$?

I risultati numerici sul 3d sono ancora incompleti, sto aspettando che finiscano di girare, però si hanno già buone conferme da quei pochi che ci sono.
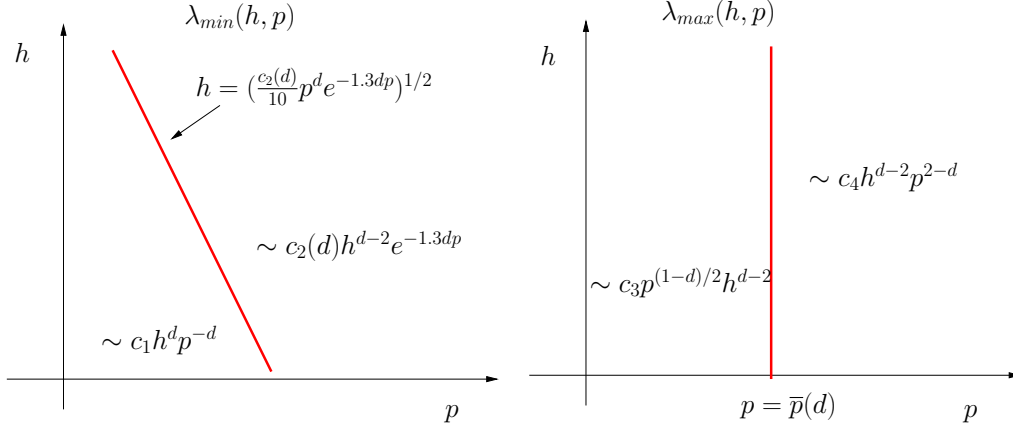
Figure 13: Behaviour of the extreme eigenvalues of the stiffness matrix of IGA-C^0 (logarithmic scale in h is used)

In Figures $15 - 20$ we show the computed eigenvalues (at left) and the right hand sides of (60) – (61) w.r.t. h and p. We deduce from numerical results that $\overline{p} = 2$ for $d = 1$, $\overline{p} = 3$ for $d = 2$, and $\overline{p} = 0$ for $d = 3$.
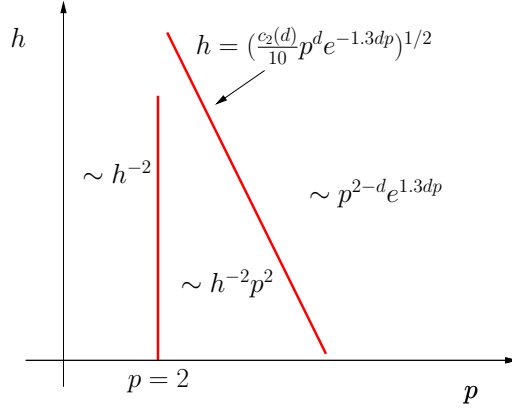
Figure 14: $\mathcal{K}(K_0)$ (logarithmic scale in h is used)

Figure 15: At left, the numerically computed values of $\lambda_{min}(K_0)$ for $d = 1$ and for different values of h and p. At right, the graphical representation of the r.h.s. of (60). The red line separates the two different regimes
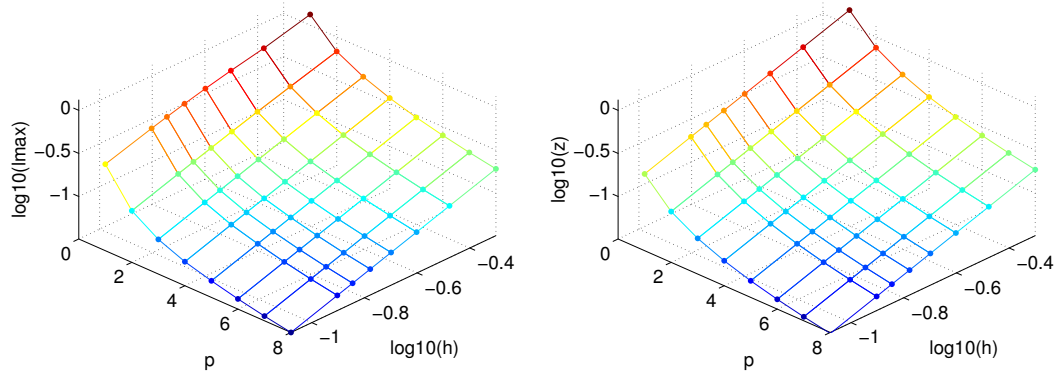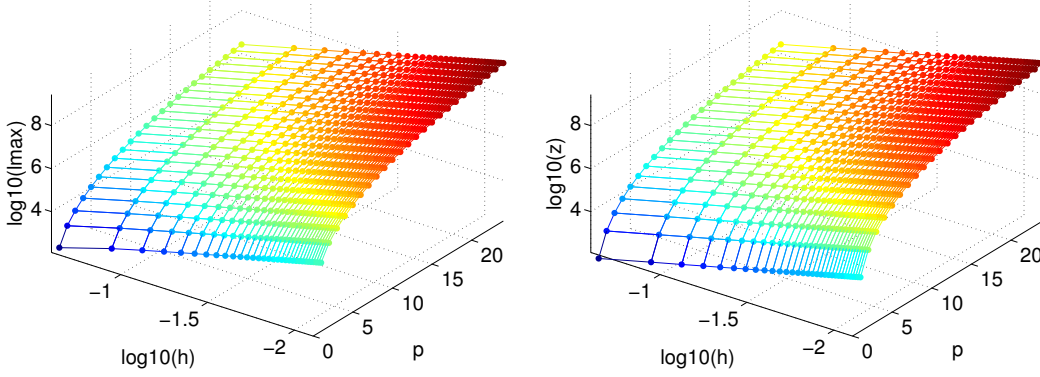
Figure 16: At left, the numerically computed values of $\lambda_{max}(K_0)$ for $d = 1$ and for different values of h and p. At right, the graphical representation of the r.h.s. of (61)
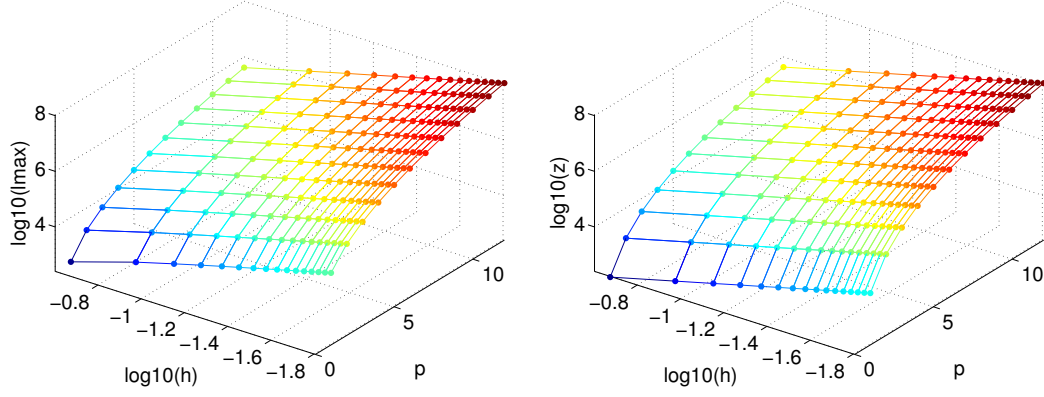

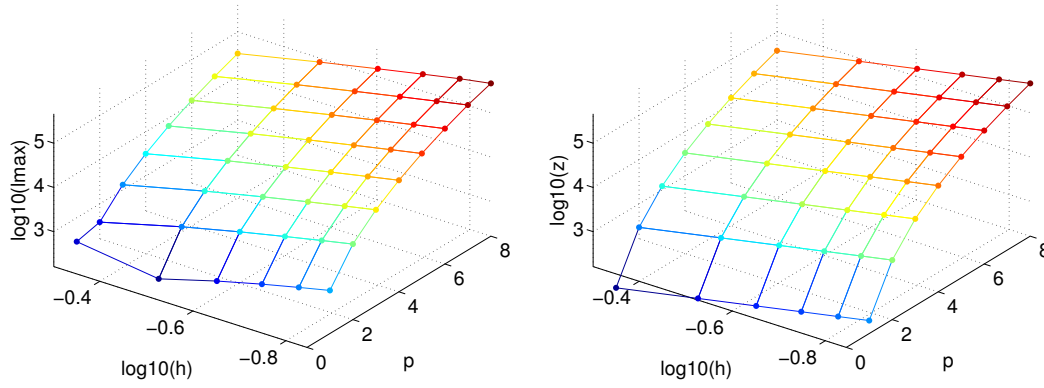Figure 17: At left, the numerically computed values of $\lambda_{min}(K_0)$ for $d = 2$ and for different values of h and p. At right, the graphical representation of the r.h.s. of (60). The red line separates the two different regimes

Figure 18: At left, the numerically computed values of $\lambda_{max}(K_0)$ for $d = 2$ and for different values of h and p. At right, the graphical representation of the r.h.s. of (61)
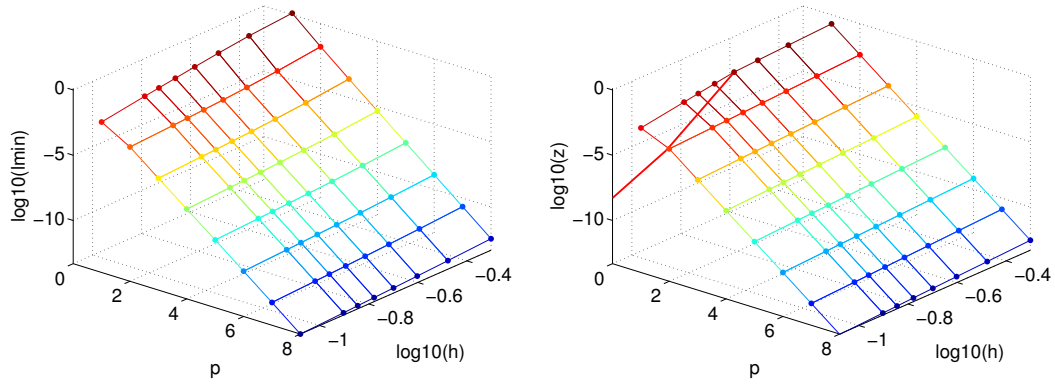
Figure 19: At left, the numerically computed values of $\lambda_{min}(K_0)$ for $d = 3$ and for different values of h and p. At right, the graphical representation of the r.h.s. of (60). The red line separates the two different regimes

Figure 20: At left, the numerically computed values of $\lambda_{max}(K_0)$ for $d = 3$ and for different values of h and p. At right, the graphical representation of the r.h.s. of (61)

4.3   IGA-C^0 $(M^{-1}K)$ matrix

The minimum eigenvalue of the matrix $(M_0)^{-1}K_0$ of IGA-C^0 is $\lambda_{min}((M_0)^{-1}K_0) \sim c$, while the maximum on behaves like

$$\lambda_{max}((M_0)^{-1}K_0) \sim c(d)p^{3.5}h^{-2} \tag{62}$$

independently of the dimension d. The constants behave as $c(d) \sim (4d+1)/2$.

In Figures 21 – 23 we show the numerically computed maximum eigenvalues (at left) and the right hand sides of (62) w.r.t. h and p.
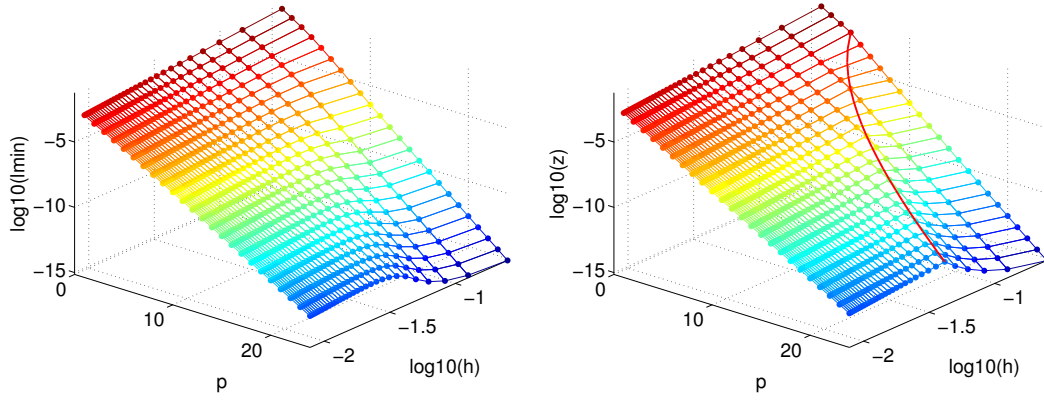

Figure 21: At left, the numerically computed values of $\lambda_{max}((M_0)^{-1}K_0)$ for $d = 1$ and for different values of h and p. At right, the graphical representation of the r.h.s. of (62)

Figure 22: At left, the numerically computed values of $\lambda_{max}((M_0)^{-1}K_0)$ for $d = 2$ and for different values of h and p. At right, the graphical representation of the r.h.s. of (62)
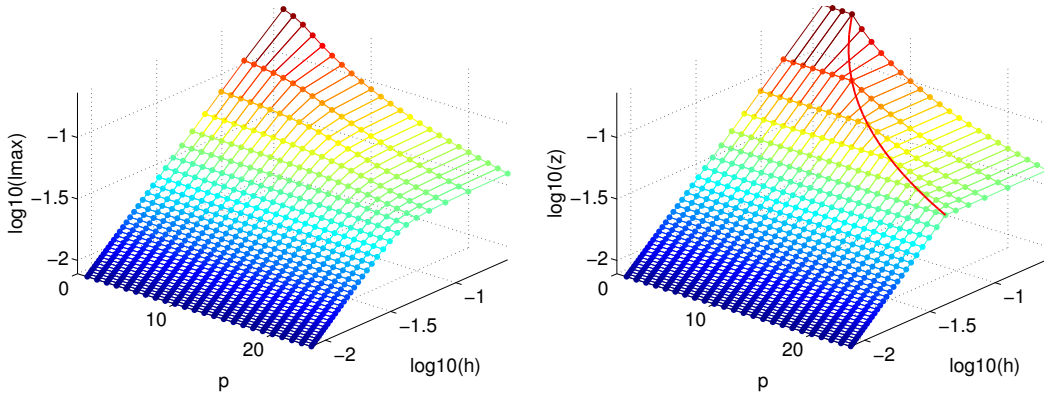

Figure 23: At left, the numerically computed values of $\lambda_{max}((M_0)^{-1}K_0)$ for $d = 3$ and for different values of h and p. At right, the graphical representation of the r.h.s. of (62)

4.4   IGA-C^{p-1} mass matrix

The extreme eigenvalues of the mass matrix M_{p-1} of IGA-C^{p-1}, behave depending on h and p, as follows (see also Fig. 24):

$$\lambda_{min}(M_{p-1}) \quad \sim \quad \begin{cases} h^d e^{-pd} & \text{if } h \leq 1/p \\ \left(\frac{e}{4}\right)^{-d/h} p^{-d} 4^{-pd} & \text{otherwise} \end{cases} \tag{63}$$

$$\lambda_{max}(M_{p-1}) \quad \sim \quad \begin{cases} h^d & \text{if } h \leq 1/p \\ p^{-d} & \text{otherwise} \end{cases} \tag{64}$$

for any $d = 1, 2, 3$.

The spectral condition number reads

$$\mathcal{K}(M_{p-1}) \quad \sim \quad \begin{cases} e^{pd} & \text{if } h \leq 1/p \\ \left(\frac{e}{4}\right)^{d/h} 4^{pd} & \text{otherwise.} \end{cases} \tag{65}$$
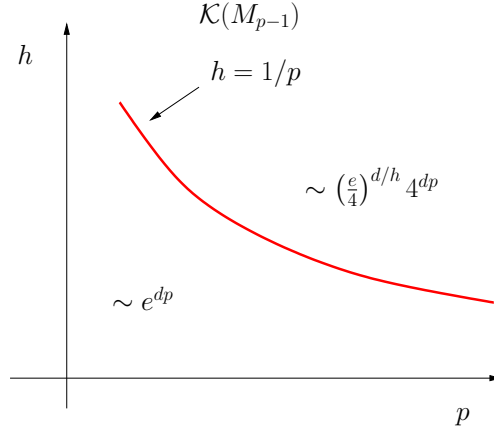
Figure 24: Behaviour of the extreme eigenvalues of the stiffness matrix of IGA-C^{p-1} (logarithmic scale in h is used)

In Figures 25 – 30 we show the numerically computed eigenvalues (at left) and the right hand sides of (63) – (64) w.r.t. h and p.
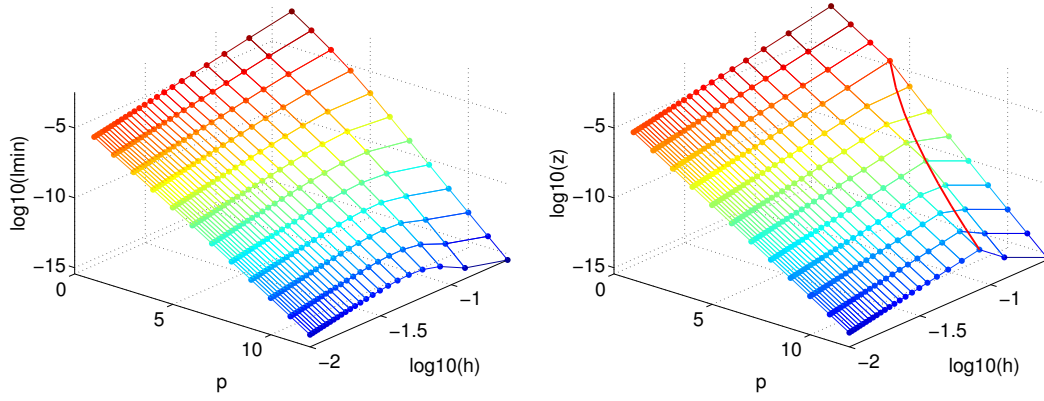
Figure 25: At left, the numerically computed values of $\lambda_{min}(M_{p-1})$ for $d = 1$ and for different values of h and p. At right, the graphical representation of the r.h.s. of (63). The red line separates the two different regimes
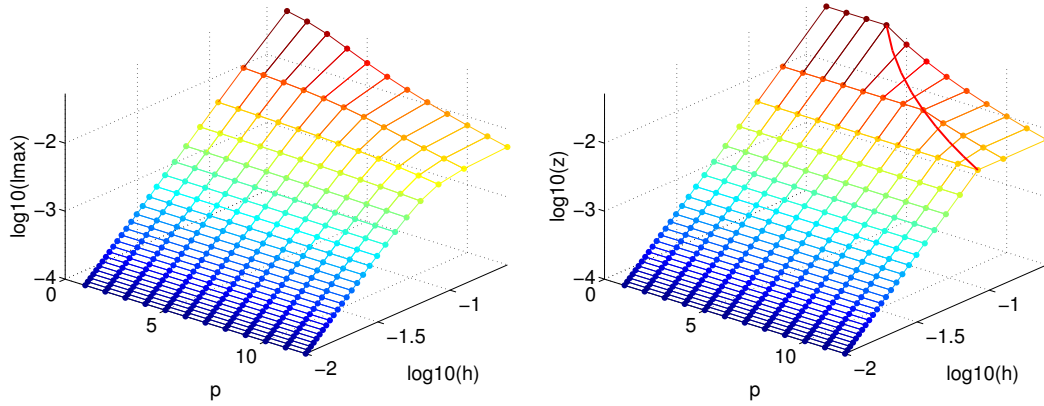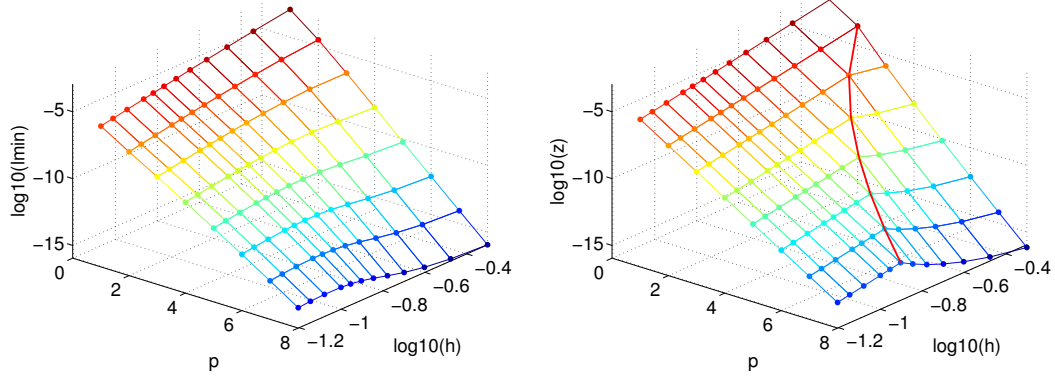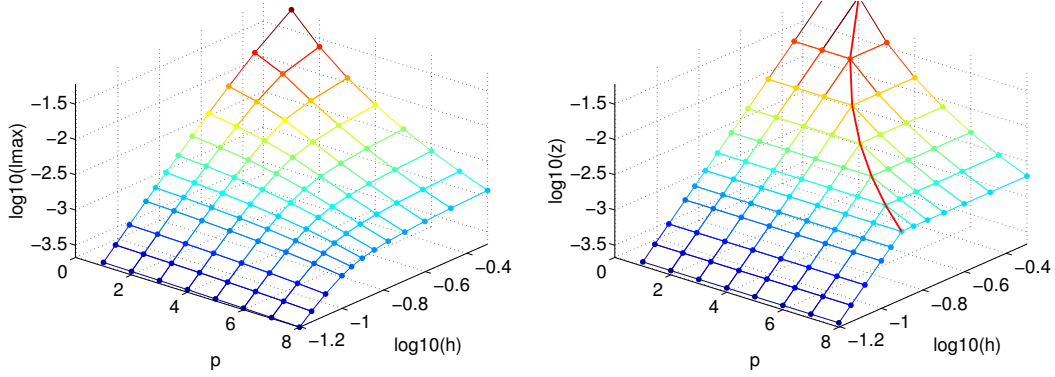

Figure 26: At left, the numerically computed values of $\lambda_{max}(M_{p-1})$ for $d = 1$ and for different values of h and p. At right, the graphical representation of the r.h.s. of (64)

Figure 27: At left, the numerically computed values of $\lambda_{min}(M_{p-1})$ for $d = 2$ and for different values of h and p. At right, the graphical representation of the r.h.s. of (63). The red line separates the two different regimes

Figure 28: At left, the numerically computed values of $\lambda_{max}(M_{p-1})$ for $d = 2$ and for different values of h and p. At right, the graphical representation of the r.h.s. of (64)

32

Figure 29: At left, the numerically computed values of $\lambda_{min}(M_{p-1})$ for $d = 3$ and for different values of h and p. At right, the graphical representation of the r.h.s. of (63). The red line separates the two different regimes

Figure 30: At left, the numerically computed values of $\lambda_{max}(M_{p-1})$ for $d = 3$ and for different values of h and p. At right, the graphical representation of the r.h.s. of (64)

33

4.5 IGA-C^{p-1} stiffness matrix

The extreme eigenvalues of the stiffness matrix K_{p-1} of IGA-C^{p-1}, behave depending on h and p, as follows (see also Fig. 24):

$$
\lambda_{min}(K_{p-1}) \quad \sim \quad
\begin{cases}
ch^d & \text{if } h \le e^{-pd/2} \\
ch^{d-2}e^{-pd} & \text{if } e^{-pd/2} \le h \le 1/p \\
c\left(\frac{e}{4}\right)^{-d/h} p^{2-d} 4^{-pd} & \text{if } h > 1/p
\end{cases}
\tag{66}
$$

$$
\lambda_{max}(K_{p-1}) \quad \sim \quad
\begin{cases}
ch^{d-2} & \text{if } p = 1 \\
cph^{d-2} & \text{if } p \ge 2 \text{ and } h \le 1/p \\
cp^{2-d}h^{-1} & \text{if } p \ge 2 \text{ and } h > 1/p
\end{cases}
\tag{67}
$$

for any $d = 1, 2, 3$.

The behaviour of the condition number $\mathcal{K}(K_{p-1})$ versus both h and p is shown in Fig. 32
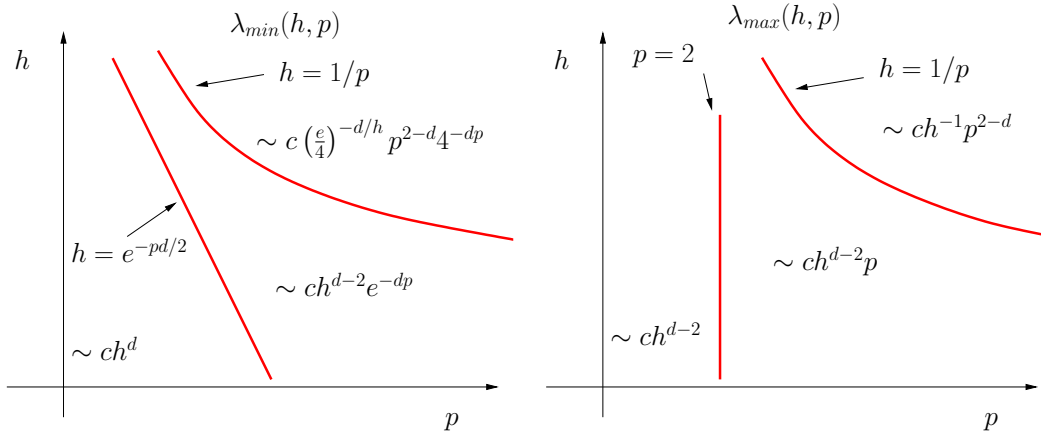
Figure 31: Stiffness matrix for IGA-C^{p-1} (logarithmic scale in h is used)
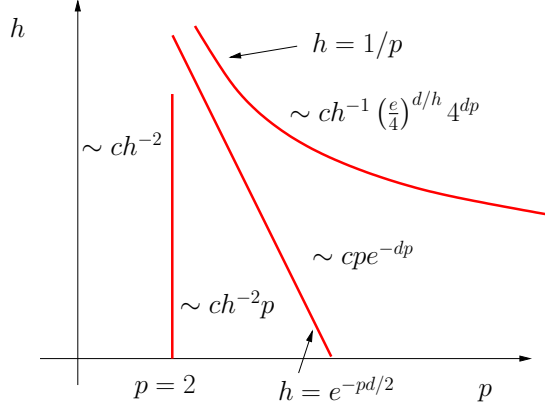
34

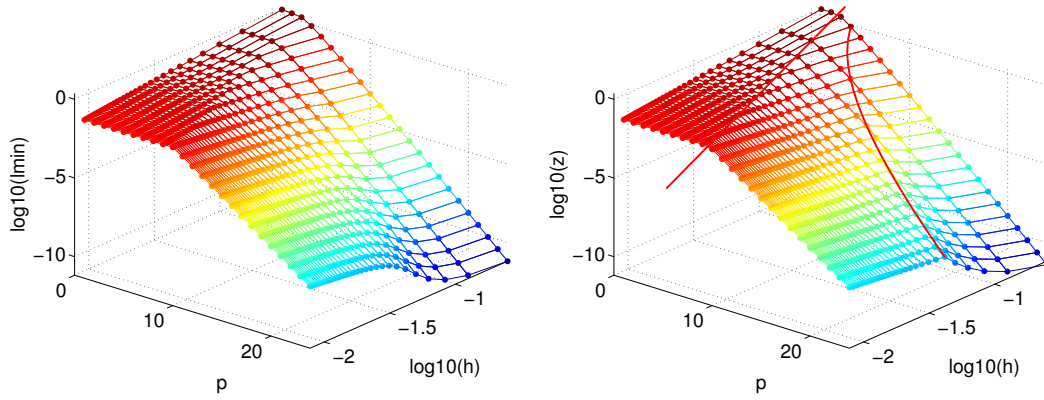Figure 32: $\mathcal{K}(K_{p-1})$ (logarithmic scale in h is used)

Figure 33: At left, the numerically computed values of $\lambda_{min}(K_{p-1})$ for $d = 1$ and for different values of h and p. At right, the graphical representation of the right hand side of (66). The red line separates the two different regimes
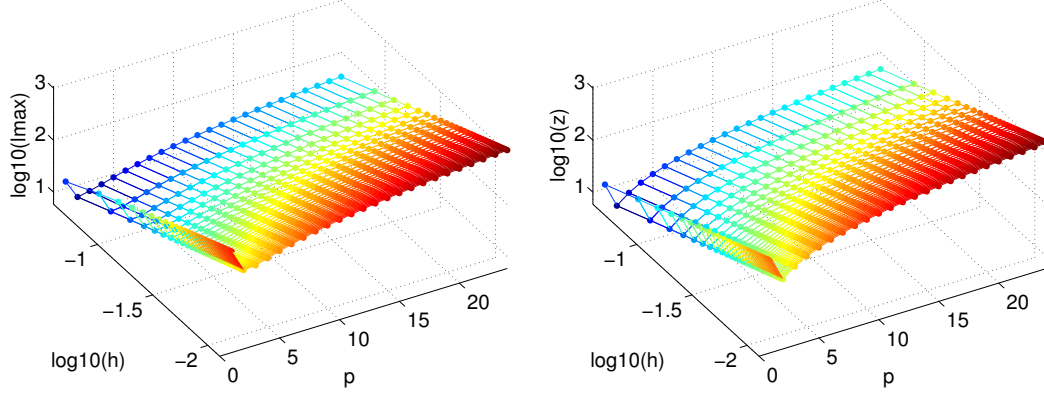
35

Figure 34: At left, the numerically computed values of $\lambda_{max}(K_{p-1})$ for $d = 1$ and for different values of h and p. At right, the graphical representation of the r.h.s. of (67)
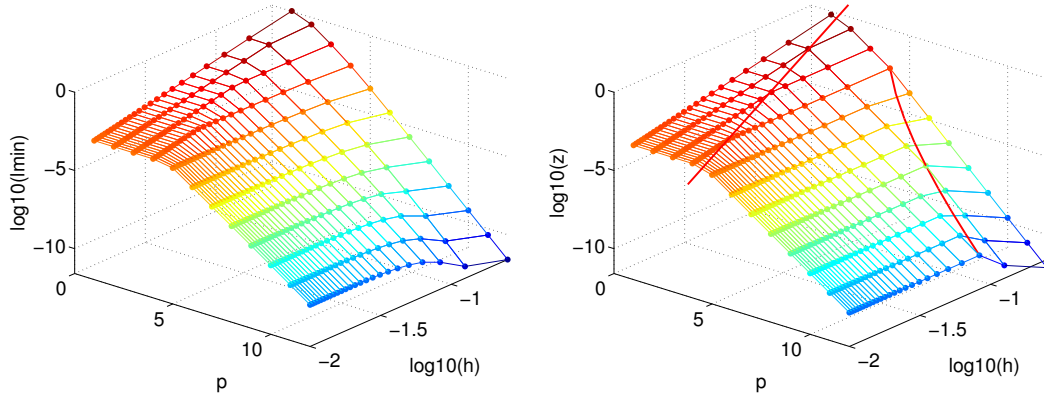

Figure 35: At left, the numerically computed values of $\lambda_{min}(K_{p-1})$ for $d = 2$ and for different values of h and p. At right, the graphical representation of the r.h.s. of (66). The red line separates the two different regimes
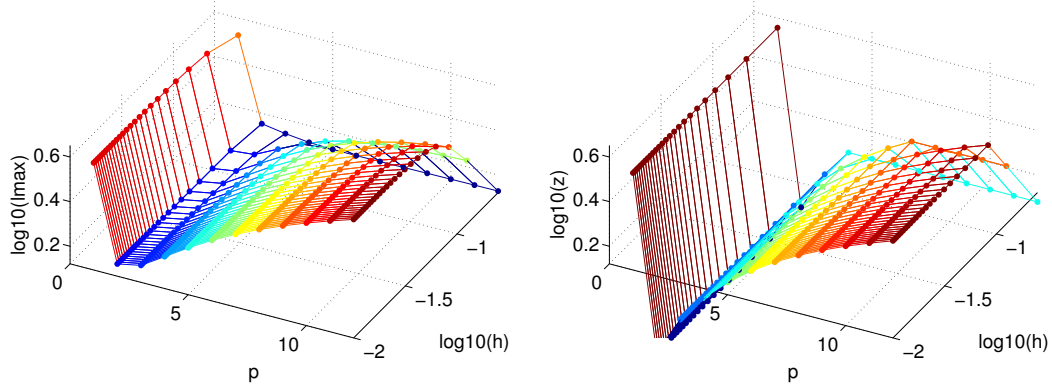
Figure 36: At left, the numerically computed values of $\lambda_{max}(K_{p-1})$ for $d = 2$ and for different values of h and p. At right, the graphical representation of the r.h.s. of (67)
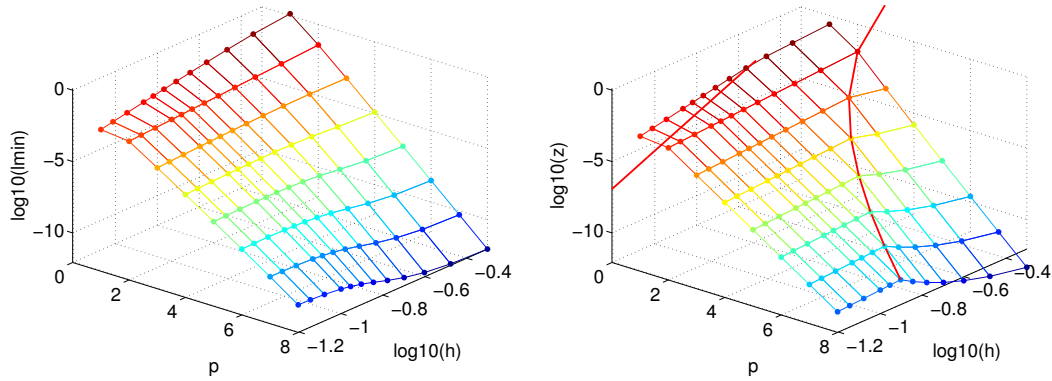

Figure 37: At left, the numerically computed values of $\lambda_{min}(K_{p-1})$ for $d = 3$ and for different values of h and p. At right, the graphical representation of the r.h.s. of (66). The red line separates the two different regimes
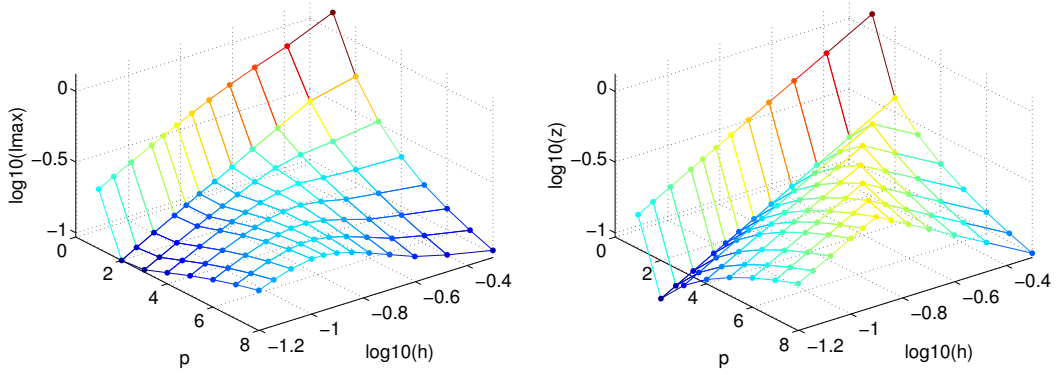
Figure 38: At left, the numerically computed values of $\lambda_{max}(K_{p-1})$ for $d = 3$ and for different values of h and p. At right, the graphical representation of the r.h.s. of (67)

4.6 IGA-C^{p-1} $M^{-1}K$ matrix

The minimum eigenvalue of the matrix $(M_{p-1})^{-1}K_{p-1}$ of IGA-C^{p-1} is $\lambda_{min}(M_{p-1})^{-1}K_{p-1} \sim c$, while the maximum one satisfies

$$\lambda_{max}((M_{p-1})^{-1}K_{p-1}) \sim c(d)p^{2.5}h^{-2} \tag{68}$$

independently of the dimension d. The constants are $c(d) \sim 2d/3$.

In Figures 39 – 41 we show the numerically computed maximum eigenvalues (at left) and the right hand sides of (68) w.r.t. h and p.
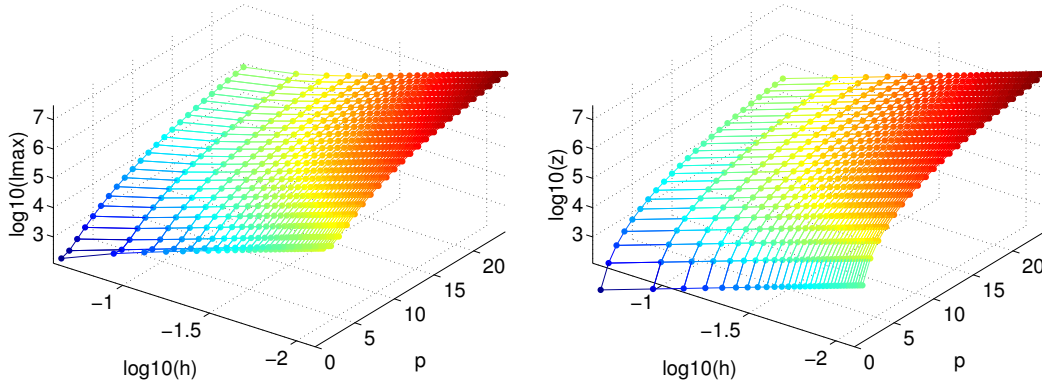

Figure 39: At left, the numerically computed values of $\lambda_{max}((M_0)^{-1}K_0)$ for $d = 1$ and for different values of h and p. At right, the graphical representation of the r.h.s. of (68)

References

[1] L. Beirão da Veiga, D. Cho, L. F. Pavarino, and S. Scacchi. BDDC preconditioners for isogeometric analysis. *Math. Models Methods Appl. Sci.*, 23(6):1099–1142, 2013.

[2] L. Beirão da Veiga, D. Cho, L. F. Pavarino, and S. Scacchi. Isogeometric Schwarz preconditioners for linear elasticity systems. *Comput. Methods Appl. Mech. Engrg.*, 253:439–454, 2013.

[3] L. Beirão da Veiga, D. Cho, L. F. Pavarino, and S. Scacchi. Overlapping Schwarz preconditioners for isogeometric collocation methods. *Comput. Methods Appl. Mech. Engrg.*, 278:239–253, 2014.

[4] L. Beirão da Veiga, L. F. Pavarino, S. Scacchi, O. B. Widlund, and S. Zampini. Isogeometric BDDC preconditioners with deluxe scaling. *SIAM J. Sci. Comput.*, 36(3):A1118–A1139, 2014.

[5] C. Bernardi and Y. Maday. *Approximations Spectrales de Problèmes aux Limites Elliptiques*. Springer Verlag, Paris, 1992.
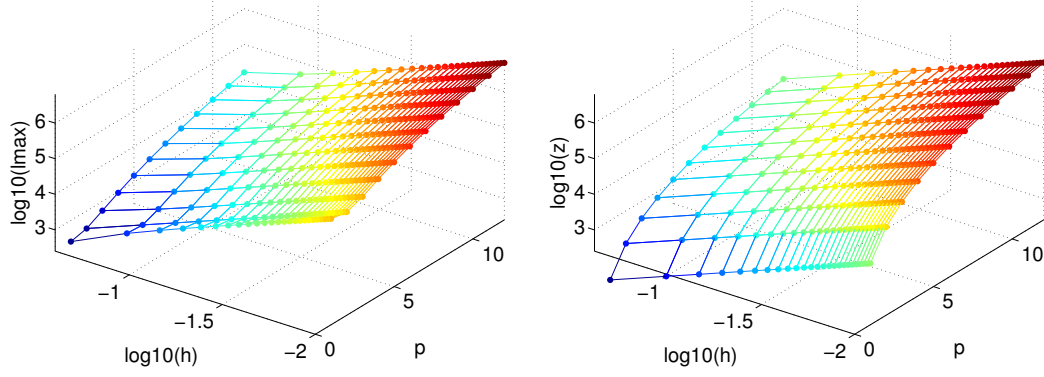
Figure 40: At left, the numerically computed values of $\lambda_{max}((M_{p-1})^{-1}K_{p-1})$ for $d = 2$ and for different values of h and p. At right, the graphical representation of the r.h.s. of (68)
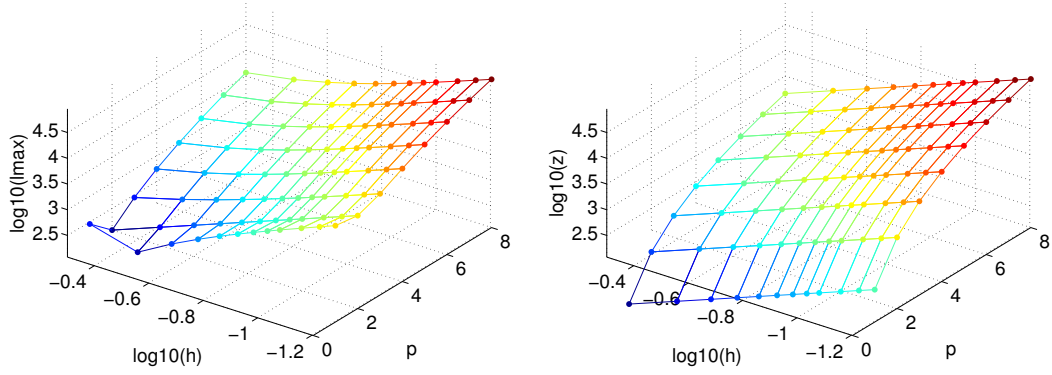

Figure 41: At left, the numerically computed values of $\lambda_{max}((M_{p-1})^{-1}K_{p-1})$ for $d = 3$ and for different values of h and p. At right, the graphical representation of the r.h.s. of (68)

[6] C. Bernardi and Y. Maday. Spectral methods. In *Handbook of numerical analysis, Vol. V*, Handb. Numer. Anal., V, pages 209–485. North-Holland, Amsterdam, 1997.

[7] C. Canuto, M. Y. Hussaini, A. Quarteroni, and T. A. Zang. *Spectral Methods. Fundamentals in Single Domains*. Springer, Heidelberg, 2006.

[8] C. Canuto, M. Y. Hussaini, A. Quarteroni, and T. A. Zang. *Spectral Methods. Evolution to Complex Geometries and Applications to Fluid Dynamics*. Springer, Heidelberg, 2007.

[9] L. Beirão da Veiga, A. Buffa, J. Rivas, and G. Sangalli. Some estimates for *h-p-k*-refinement in isogeometric analysis. *Numer. Math.*, 118(2):271–305, 2011.

[10] L. Beirão da Veiga, A. Buffa, G. Sangalli, and R. Vàzquez. An introduction to the numerical analysis of isogeometric methods. In *Numerical simulation in physics and engineering*, volume 9 of *SEMA SIMAI Springer Ser.*, pages 3–69. Springer, [Cham], 2016.

[11] L. Beirão da Veiga, L.F. Pavarino, S. Scacchi, O.B. Widlund, and S. Zampini. Adaptive selection of primal constraints for isogeometric BDDC deluxe preconditioners. *SIAM J. Sci. Comput.*, 39(1):A281–A302, 2017.

[12] K. Gahalaut and S. Tomar. Condition number estimates for matrices arising in the isogeometric discretizations. Technical Report 2012-23, RICAM, 2012.

[13] C. Garoni, C. Manni, F. Pelosi, S. Serra-Capizzano, and H. Speleers. On the spectrum of stiffness matrices arising from isogeometric analysis. *Numer. Math.*, 127(4):751–799, 2014.

[14] Y. Bazilevs J.A. Cottrell, T.J.R. Hughes. *Isogeometric Analysis: Toward Integration of CAD and FEA*. Wiley, 2009.

[15] J.M. Melenk. On condition numbers in *hp*-FEM with Gauss-Lobatto-based shape functions. *J. Comput. Appl. Math.*, 139(1):21–48, 2002.

[16] L.F. Pavarino and S. Scacchi. Isogeometric block FETI-DP preconditioners for the Stokes and mixed linear elasticity systems. *Comput. Methods Appl. Mech. Engrg.*, 310:694–710, 2016.

[17] A. Quarteroni and A. Valli. *Numerical Approximation of Partial Differential Equations*. Springer Verlag, Heidelberg, 1994.

[18] G. Sangalli and M. Tani. Isogeometric preconditioners based on fast solvers for the Sylvester equation. *SIAM J. Sci. Comput.*, 38(6):A3644–A3671, 2016.

[19] H.A. van der Vorst. *Iterative Krylov methods for large linear systems*. Cambridge University Press, Cambridge, 2003.